Molecular Therapy
Original Article

A small TAT-TrkB peptide prevents BDNF receptor cleavage and restores synaptic physiology in Alzheimer's disease

João Fonseca-Gomes,[1,2,22,20] Tiago Costa-Coelho,[1,2,3,20] Mafalda Ferreira-Manso,[1,2,3,4,20] Sara Inteiro-Oliveira,[1,2,20] Sandra H. Vaz,[1,2] Nuno Alemãn-Serrano,[1,2,23] Henrique Atalaia-Barbacena,[1,2] Leonor Ribeiro-Rodrigues,[1,2] Rita M. Ramalho,[1,2,24] Rui Pinto,[5,6] Hugo Vicente Miranda,[7] Sara R. Tanqueiro,[1,2] Carolina de Almeida-Borlido,[1,2] Maria João Ramalho,[8,9] Catarina Miranda-Lourenço,[1,2] Rita F. Belo,[1,2] Catarina B. Ferreira,[1,2] Vera Neves,[2] Diogo M. Rombo,[1,2] Ricardo Viais,[1,2] Ivo C. Martins,[2] André Jerónimo-Santos,[1,2] António Caetano,[1,2] Nuno Manso,[1] Petra Mäkinen,[10] Mikael Marttinen,[10,11] Mari Takalo,[10] Michael Bremang,[12] Ian Pike,[12] Annakaisa Haapasalo,[13] Joana A. Loureiro,[8,9] Maria Carmo Pereira,[8,9] Nuno C. Santos,[2] Tiago F. Outeiro,[14,15,16,17] Miguel A.R.B. Castanho,[2] Adelaide Fernandes,[3,4] Mikko Hiltunen,[10] Carlos B. Duarte,[18] Eero Castrén,[19] Alexandre de Mendonça,[1] Ana M. Sebastião,[1,2] Tiago M. Rodrigues,[1,2,25,21] and Maria José Diógenes[1,2,21]

[1]Instituto de Farmacologia e Neurociências, Faculdade de Medicina, Universidade de Lisboa, 1649-028 Lisbon, Portugal; [2]Instituto de Medicina Molecular João Lobo Antunes, Faculdade de Medicina, Universidade de Lisboa, 1649-028 Lisbon, Portugal; [3]Research Institute for Medicines (iMed.ULisboa), Faculdade de Farmácia, Universidade de Lisboa, 1649-003 Lisbon, Portugal; [4]Department of Pharmaceutical Sciences and Medicines, Faculdade de Farmácia, Universidade de Lisboa, 1649-003 Lisbon, Portugal; [5]Laboratory of Systems Integration Pharmacology, Clinical, and Regulatory Science, Research Institute for Medicines (iMED.ULisboa), Faculdade de Farmácia, Universidade de Lisboa, 1649-003 Lisbon, Portugal; [6]Dr. Joaquim Chaves Laboratório de Análises Clínicas, 2790-224 Carnaxide, Portugal; [7]iNOVA4Health, NOVA Medical School, NMS, Universidade NOVA de Lisboa, 1169-056 Lisbon, Portugal; [8]LEPABE – Laboratory for Process Engineering, Environment, Biotechnology, and Energy, Faculty of Engineering, University of Porto, 4200-465 Porto, Portugal; [9]ALiCE—Associate Laboratory in Chemical Engineering, Faculty of Engineering, University of Porto, 4200-465 Porto, Portugal; [10]Institute of Biomedicine, School of Medicine, University of Eastern Finland, P.O. Box 1627, 70211 Kuopio, Finland; [11]Structural and Computational Biology, European Molecular Biology Laboratory, 69117 Heidelberg, Germany; [12]Proteome Sciences, Coveham House, Downside Bridge Road, KT11 3EP Cobham, UK; [13]A.I. Virtanen Institute for Molecular Sciences, University of Eastern Finland, 70211 Kuopio, Finland; [14]Department of Experimental Neurodegeneration, Center for Biostructural Imaging of Neurodegeneration, University Medical Center Göttingen, 37073 Göttingen, Germany; [15]Max Planck Institute for Experimental Medicine, 37075 Göttingen, Germany; [16]Translational and Clinical Research Institute, Faculty of Medical Sciences, Newcastle University, Newcastle upon Tyne NE1 7RU, UK; [17]German Center for Neurodegenerative Diseases (DZNE), 37075 Göttingen, Germany; [18]CNC – Center for Neuroscience and Cell Biology and Department of Life Sciences, University of Coimbra, 3004-504 Coimbra, Portugal; [19]Neuroscience Center, University of Helsinki, 00014 Helsinki, Finland

In Alzheimer's disease (AD), amyloid β (Aβ)-triggered cleavage of TrkB-FL impairs brain-derived neurotrophic factor (BDNF) signaling, thereby compromising neuronal survival, differentiation, and synaptic transmission and plasticity. Using cerebrospinal fluid and postmortem human brain samples, we show that TrkB-FL cleavage occurs from the early stages of the disease and increases as a function of pathology severity. To explore the therapeutic potential of this disease mechanism, we designed small TAT-fused peptides and screened their ability to prevent TrkB-FL receptor cleavage. Among these, a TAT-TrkB peptide with a lysine-lysine linker prevented TrkB-FL cleavage both *in vitro* and *in vivo* and rescued synaptic deficits induced by oligomeric Aβ in hippocampal slices. Furthermore, this TAT-TrkB peptide improved the cognitive performance, ameliorated synaptic plasticity deficits and prevented Tau pathology progression *in vivo* in the 5XFAD mouse model of AD. No evidence of liver or kidney toxicity was found. We

Received 20 January 2024; accepted 23 August 2024;
https://doi.org/10.1016/j.ymthe.2024.08.022.

[20]These authors contributed equally

[21]These authors contributed equally

[22]Present address: Roche Farmacêutica e Química, 2720-413 Amadora, Portugal

[23]Present address: ULS Santa Maria, Centro Académico de Medicina de Lisboa, 1649-028 Lisbon, Portugal

[24]Present address: Serviço de Patologia Clínica, Instituto Português de Oncologia de Lisboa Francisco Gentil, 1099-023 Lisbon, Portugal

[25]Present address: Institute of Molecular and Clinical Ophthalmology Basel (IOB), 4031 Basel, Switzerland

Correspondence: Tiago M. Rodrigues, Institute of Molecular and Clinical Ophthalmology Basel (IOB), 4031 Basel, Switzerland.
E-mail: tiago.rodrigues@iob.ch
Correspondence: Maria José Diógenes, Instituto de Farmacologia e Neurociências, Faculdade de Medicina, Universidade de Lisboa, 1649-028 Lisbon, Portugal.
E-mail: diogenes@medicina.ulisboa.pt

provide proof-of-concept evidence for the efficacy and safety of this therapeutic strategy and anticipate that this TAT-TrkB peptide has the potential to be a disease-modifying drug that can prevent and/or reverse cognitive deficits in patients with AD.

INTRODUCTION

The brain-derived neurotrophic factor (BDNF) and its full-length canonical receptor, TrkB-FL, constitute one of the most important endogenous neuroprotective systems.[1] Dysregulation of BDNF function has been implicated in several diseases, including Alzheimer's disease (AD).

AD is the prototypical neurodegenerative disorder that causes cognitive decline and dementia. It is the most common form of dementia (≈75% of all dementia cases), affecting about 47 million people worldwide, and this number is estimated to increase to 152 million by 2050.[2] It initially manifests itself with episodic memory loss, but subsequently progresses to affect most cognitive functions, including language, attention, abstraction and reasoning.[3]

Senile plaques, which comprise large extracellular aggregates of insoluble fibrillar amyloid β peptide (Aβ),[4] and intracellular tangles of hyperphosphorylated Tau (p-Tau)[5] are recognized as the histopathological hallmarks of AD. Neurofibrillary tangles are thought to be bystanders[6] or mediators[7] of Aβ toxicity, thus putatively placing Aβ at the top of the pathological chain of events. Aβ is produced by the proteolytic cleavage of the amyloid precursor protein (APP) by β- and γ-secretases.[8] Although initially present as monomers, Aβ readily aggregates to form intermediate species (e.g., oligomers, protofibrils) and, ultimately, the more stable and insoluble fibrils.[9]

BDNF and TrkB-FL mRNA and protein levels were shown to be decreased in the brain of AD patients when compared to healthy controls.[10–15] We previously described the mechanism of Aβ-mediated TrkB-FL cleavage. Briefly, the Aβ peptide promotes an increase in intracellular Ca^{2+} levels through a mechanism dependent on *N*-methyl-D-aspartate (NMDA) receptors, which leads to calpain overactivation and TrkB-FL proteolytic cleavage.[16,17] This cleavage produces a membrane-bound truncated receptor (TrkB-T′) and an intracellular fragment (TrkB-ICD), the latter accumulating in the nucleus and displaying tyrosine kinase activity.[18]

In this work, we aimed to leverage this knowledge to design a new therapeutic strategy for AD and to provide proof-of-concept results of its efficacy and safety. First, we demonstrate that TrkB-FL cleavage is a relevant mechanism for human disease by examining protein levels in cerebrospinal fluid (CSF) samples and the protein and mRNA profiles of postmortem AD human brains. Second, we show that TrkB-ICD overexpression caused dendritic spine loss and altered excitatory synaptic transmission, and it impacted the transcriptomic profile of synapse-related genes in primary cultured neurons. Third, with the aim of preventing TrkB-FL cleavage and TrkB-ICD formation, we designed peptides spanning the cleavage site of TrkB and fused to the TAT (Trans-Activator of Transcription) sequence, analyzed their conformational stability *in silico*, and used *in vitro* assays to screen their efficacy. Subsequently, we used the rodent hippocampus to investigate the effects of the TAT-TrkB peptide on BDNF signaling under Aβ-toxic conditions *ex vivo*, using core readouts of neuronal function (synaptic transmission, plasticity, and neurotransmitter release). Finally, we administered TAT-TrkB to the 5XFAD mouse model of AD to examine its *in vivo* efficacy to prevent TrkB-FL cleavage, improve cognitive performance, ameliorate synaptic plasticity deficits, impact Aβ and p-Tau pathology, and identify potential systemic side effects.

RESULTS

TrkB-FL cleavage is a hallmark of AD-related pathology progression in humans, and it correlates with the levels of $A\beta_{1-42}$, but not of hyperphosphorylated Tau

The decreased expression of BDNF and TrkB-FL in the brains of AD patients can either be (1) mechanistically implicated or (2) a by-product of AD progression. To address this question, we examined the status of TrkB-FL cleavage in samples from human patients with AD-related pathology at different stages of disease severity. We evaluated TrkB-FL cleavage in CSF samples from three groups of human patients with (1) mild cognitive impairment (MCI), but no evidence of Aβ deposition or neuronal injury (MCI controls), (2) MCI due to AD-high likelihood, or (3) frontotemporal dementia (FTD). Compared to MCI controls, patients with MCI due to AD showed increased levels of TrkB-ICD fragment and of the TrkB-ICD:TrkB-FL ratio, even though no significant changes in TrkB-FL levels were found (Figures S1A–S1D). As expected, CSF levels of $A\beta_{1-42}$ were significantly decreased (Figure S1E), while the levels of total Tau (t-Tau) and p-Tau were both increased (Figures S1F and S1G). We then tested pairwise correlations between the levels of BDNF/TrkB and the levels of molecular AD hallmarks ($A\beta_{1-42}$ and Tau) and age. Only the correlation between the levels of TrkB-ICD and $A\beta_{1-42}$ in the MCI due to AD group was found to be statistically significant (Figure 1A). Importantly, the levels of $A\beta_{1-42}$, but not the levels of p-Tau, were correlated with the levels of TrkB-ICD fragment and, hence, with the degree of TrkB-FL cleavage (Figures 1B and 1C). We also examined CSF samples of patients with FTD, a form of dementia that is mechanistically distinct from AD. Despite TrkB-FL immunoreactivity showing no significant change, TrkB-ICD levels were increased in samples from FTD patients (Figures S1H–S1K). CSF samples from FTD patients showed no changes in $A\beta_{1-42}$ abundance, or in p-Tau, but they did present increased CSF levels of t-Tau, compared to MCI controls (Figures S1L–S1N).

Additionally, we analyzed postmortem inferior temporal cortical parenchyma samples from human patients with AD-related pathology in different Braak stages. TrkB-FL protein levels were decreased in the later stages, compared to earlier stages of the disease (by western blot: Figures 1D and 1E; by mass spectrometry: Figure S1O). Reciprocally, we observed a significant increase in the levels of TrkB-ICD fragment (Figure 1F) and of the TrkB-ICD:TrkB-FL ratio (Figure S1P)

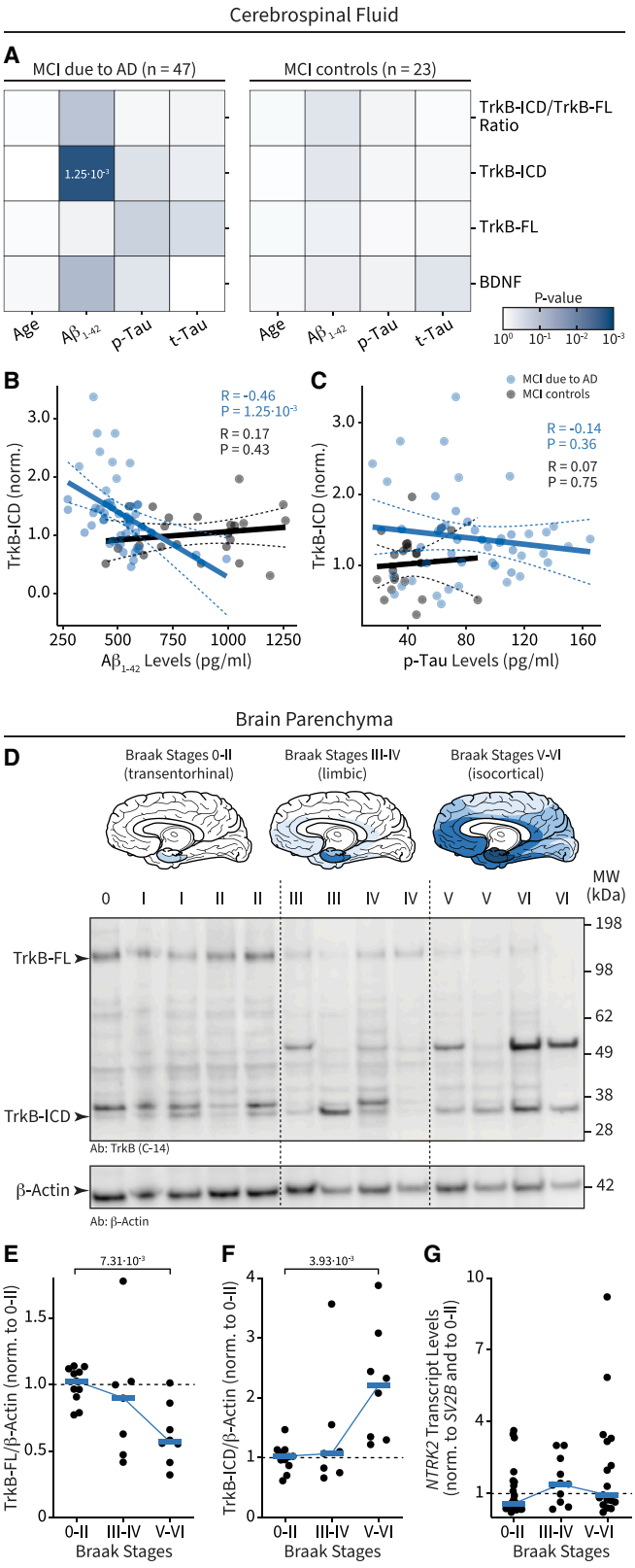

Figure 1. Cleavage of TrkB-FL is a hallmark of AD progression, and it is correlated with the levels of $A\beta_{1\text{-}42}$, even in early stages of the disease

(A) Heatmaps of pairwise correlation *p* values between parameters measured in the CSF of patients with MCI due to AD ($n = 47$) and MCI controls ($n = 23$). Correlations were evaluated between parameters related to BDNF signaling (BDNF, TrkB-FL, TrkB-ICD, and the TrkB-ICD:TrkB-FL ratio), molecular biomarkers of AD ($A\beta_{1\text{-}42}$, p-Tau, and t-Tau), and age. Only the correlation between the levels of TrkB-ICD and $A\beta_{1\text{-}42}$ in patients with MCI due to AD was found to be statistically significant ($R = -0.46$, $p = 1.25 \times 10^{-3}$, Pearson's correlation coefficient; a Bonferroni-adjusted $\alpha = 3.13 \times 10^{-3}$ was considered to account for multiple comparisons). Univariate analyses of each parameter are shown in Figures S1A–S1G. (B and C) Scatterplots depicting values of individual patients for two pairs of parameters: $A\beta_{1\text{-}42}$ versus TrkB-ICD levels (B) and p-Tau versus TrkB-ICD levels (C). Linear regressions with 95% confidence ribbons are overlaid. (D) Classification of AD pathology according to Braak staging (top). Representative western blot of human temporal cortical samples probed with anti-TrkB C-terminal and anti-β-actin antibodies (bottom). (E and F) Quantification of TrkB-FL (E) and TrkB-ICD (F) levels in human patients with AD, according to the severity of AD-related pathology. Data are normalized for group Braak stages 0–II (Braak stages 0–II: $n = 11$; III–IV: $n = 7$; V–VI: $n = 8$). Individual replicates are shown with group medians (solid lines) overlaid (E: $H = 9.26$, $p = 9.78 \times 10^{-3}$; F: $H = 11.03$, $p = 4.03 \times 10^{-3}$; Kruskal-Wallis test, followed by Dunn's test for multiple comparisons). (G) Microarray quantification of TrkB-FL transcript (*NTRK2* gene) levels normalized to the *SV2B* gene, according to disease stage. Data are normalized for group Braak stages 0–II (Braak stage 0–II: $n = 27$; III–IV: $n = 11$; V–VI: $n = 17$). Individual replicates are shown with group medians (solid lines) overlaid ($H = 5.57$, $p = 0.06$; Kruskal-Wallis test, followed by Dunn's test for multiple comparisons). See also Figure S1 and Tables S1 and S2.

with disease progression. Transcript levels of the *NTRK2* gene, which encodes the TrkB receptor, did not change significantly (Figure 1G).

TrkB-ICD overexpression causes loss of dendritic spines, alters synaptic transmission, and impacts the expression levels of synapse-related genes

Overall, the data above suggest that TrkB-FL cleavage may be implicated in the mechanisms driving AD progression by (1) compromising canonical BDNF signaling and/or (2) favoring TrkB-ICD formation, which may propagate Aβ-triggered toxicity.[16,18]

To explore the effects of excess TrkB-ICD on neuronal morphology and activity, we transduced cultured primary cortical neurons with lentiviruses (LVs) expressing TrkB-ICD (or EGFP, as a control), under the regulation of the neuron-specific CaMKIIα promoter[19] (Figure 2A). The labeling efficiency of LV-CaMKIIα-EGFP (LV-GFP) and LV-CaMKIIα-TrkB-ICD-IRES (internal ribosome entry site)-ZsGreen1 (LV-ICD) was 78% ± 6% and 77% ± 5%, respectively; of all labeled cells, 95% ± 3% and 99% ± 1% were neurons for LV-GFP- and LV-ICD-transduced cultures, respectively (Figures 2B–2E). Following transduction with LV-GFP, EGFP localized to both the somatic and dendritic compartments of neurons (Figure 2B), while, following LV-ICD transduction, TrkB-ICD expression was mainly restricted to the cell nucleus (Figure 2D), which is consistent with our previous results.[18]

To validate the model, we quantified the expression levels of TrkB-ICD through western blot analysis and found them to be significantly

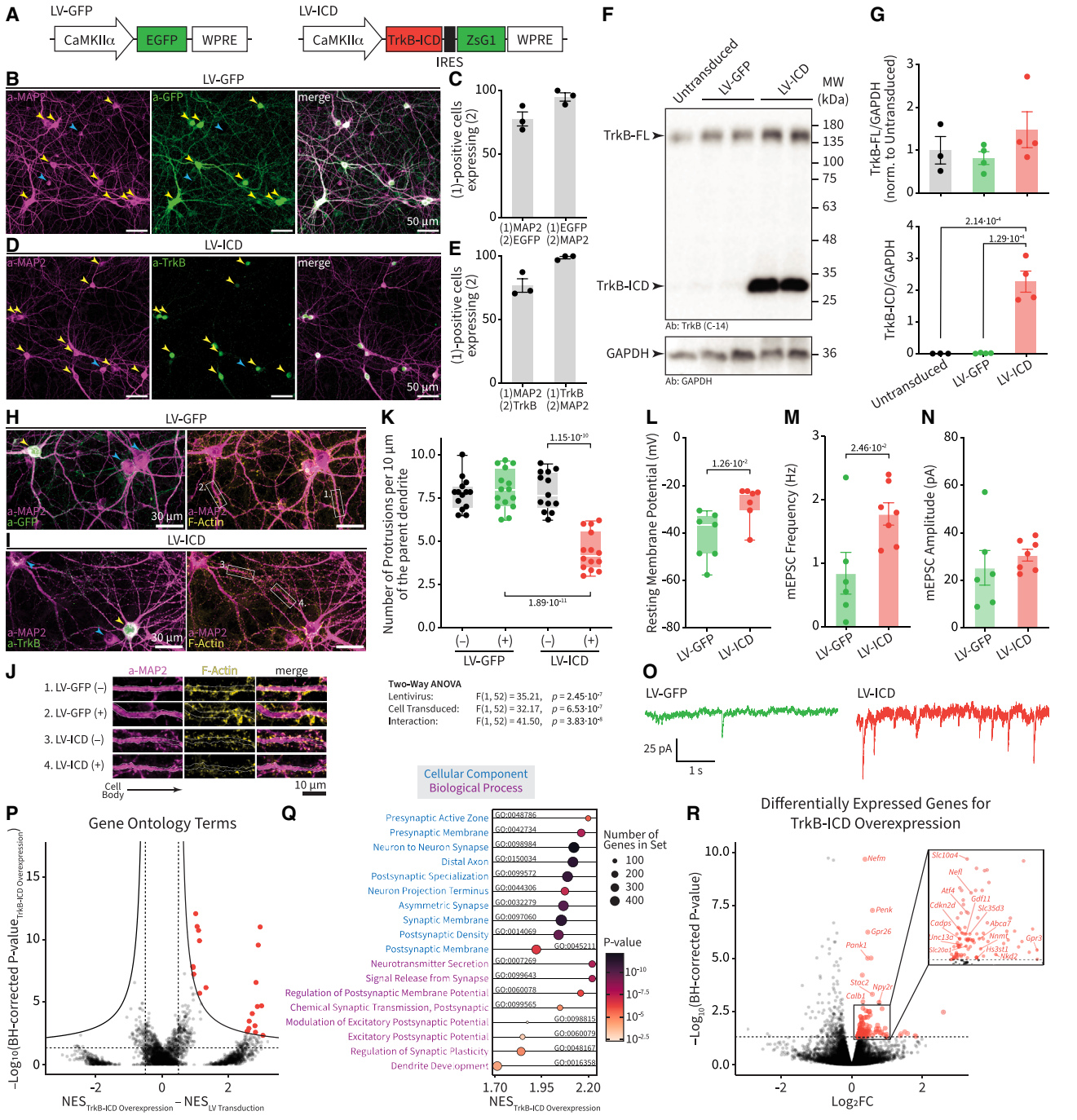

Figure 2. The cleavage product TrkB-ICD causes dendritic spine loss and neuronal hyperexcitability and changes the expression levels of synapse-related genes

(A) Schematic diagrams of the LV payload. (B–E) Representative microscopy images of primary cultured neurons (DIV14) transduced with either LV-CaMKIIα-EGFP (LV-GFP) (B) or LV-CaMKIIα-TrkB-ICD-IRES-ZsGreen1 (LV-ICD) (D). Yellow arrowheads label cells co-expressing MAP2 (a neuronal marker) and the LV payload, while blue arrowheads indicate untransduced neurons. Quantifications of transduction efficiency and neuronal selectively are shown in (C) and (E) for LV-GFP and LV-ICD, respectively ($n = 3$ independent cultures per condition). (F) Representative western blot of transduced and untransduced primary cultured neurons (DIV10) probed with anti-TrkB C-terminal and anti-GAPDH antibodies. (G) Quantification of TrkB-FL (top) and TrkB-ICD (bottom) levels in transduced and untransduced primary cultured neurons (DIV10). Individual replicates (circles) are shown with mean ± SEM (bars and error bars) overlaid ($n = 3$–4 replicates from $n = 3$ independent cultures per condition; top: $F(2,8) = 1.23$, $p = 0.34$; bottom: $F(2,8) = 39.51$, $p = 3.85 \times 10^{-3}$; one-way ANOVA, followed by Tukey's test for multiple comparisons). (H–J) Representative microscopy images of primary cultured

(legend continued on next page)

increased in neurons transduced with LV-ICD as compared to both LV-GFP-transduced and untransduced controls, while the endogenous levels of TrkB-FL were not impacted by TrkB-ICD overexpression (Figures 2F and 2G). Furthermore, we found TrkB-ICD to increase phosphorylation of tyrosine residues of several proteins (Figures S2A and S2B), as previously shown.[18]

To study the structural and functional implications of TrkB-ICD overexpression, we assessed (1) cell viability through the MTT (3-(4,5-dimethylthiazol-2-yl)-2,5-diphenyl tetrazolium bromide) assay, (2) spine density through immunocytochemistry studies, and (3) spontaneous excitatory neuronal activity through whole-cell patch-clamp recordings. While TrkB-ICD overexpression did not overtly affect cell survival (Figure S2C), it caused a significant decrease in the number of dendritic spines (4.41 ± 0.29 spines/10 μm), both compared to neighboring untransduced neurons (7.89 ± 0.31 spines/10 μm) and to LV-GFP-transduced neurons (7.97 ± 0.29 spines/10 μm) (Figures 2H–2K). Furthermore, TrkB-ICD overexpressing neurons presented a hyperpolarized resting membrane potential and an increased frequency of miniature excitatory postsynaptic currents (mEPSCs), compared to neurons transduced with LV-GFP (Figures 2L–2O).

To gain deeper insight into the underlying molecular mechanisms, we next isolated RNA from transduced and untransduced primary cortical neurons and performed high-throughput RNA sequencing (RNA-seq). A lentiviral transduction was performed in a set of two out of three conditions (LV-GFP and LV-ICD), while, in another set (untransduced and LV-GFP), TrkB-ICD was not overexpressed. This experimental design allowed us to set up the statistical contrasts in a way that distinguishes effects due to the overexpression of TrkB-ICD (specific) from effects due to the LV transduction procedure itself (unspecific) (see materials and methods section for details on the statistical framework).

First, we performed differential gene expression analysis and found 360 genes to be differentially expressed due to TrkB-ICD overexpression (at false discovery rate [FDR] <0.05), while only 58 genes changed due to the transduction procedure. Second, we performed gene set enrichment analysis and found several Gene Ontology (GO) terms enriched for both contrast levels. To discern which of these were specifically associated with TrkB-ICD overexpression, we compared the normalized enrichment scores (NESs) of all tested GO terms for both contrasts and found 23 GO terms to be specifically upregulated due to TrkB-ICD overexpression (Figure 2P). Using the same thresholds, no GO term was found to be up- or downregulated due to the LV transduction procedure (Figure S2I). The 18 terms with the highest NESs are shown in Figure 2Q, and they all encompass genes that encode for proteins that integrate synaptic structures or are directly implicated in synaptic function, such as in neurotransmitter release. The positive enrichment of these GO terms was driven by a consistent upregulation, albeit small, of many genes involved in these processes (Figures S2J and S2K). Furthermore, among the differentially expressed genes (Figure 2R), we found genes previously shown to be involved in (1) neuronal survival, growth, and differentiation (*Nkd2*, *Cend1*, *Rtn4rl1*, *Ttl*, *Gpr3*, *Ciapin1*, *Tafa2*); (2) neuronal cytoarchitecture and spine morphology (*Nefl*, *Nefm*, *Kif5c*); (3) neurodegenerative processes, including AD (*Abca7*, *Sik1*, *Hs3st1*, *Cdkn2d*, *Gpr26*, *Pank1*, *Gdf11*, *Nnmt*); and (4) synaptic transmission and plasticity (*Unc13a*, *Slc10a4*, *Cadps*, *Ddn*, *Slc35d3*, *Calb1*, *Npy2r*, *Atf4*, *Slc20a1*, *Plcl1*, *Got1*).

Overall, these results show that TrkB-ICD overexpression can cause dendritic spine loss, alter excitatory synaptic transmission, and drive transcriptome-wide changes in genes encoding for synaptic proteins.

A TAT-TrkB peptide with a lysine-lysine linker is conformationally stable and prevents TrkB-FL cleavage

To prevent the excessive accumulation of TrkB-ICD and to restore canonical BDNF signaling, we designed peptides composed of the sequence spanning the TrkB cleavage site[16] fused to the TAT protein transduction domain (TAT-TrkB; Figures 3A and S3A–S3D). By competing with TrkB-FL for calpain substrate binding, we expected TAT-TrkB to protect the BDNF receptor from cleavage. The blood-brain barrier (BBB) poses a hurdle to several drugs; therefore, we carefully designed a molecule that could be useful for *in vivo* applications, as the TAT sequence increases the capacity of proteins to diffuse across cell membranes and the BBB.[20,21]

The first TAT-0-TrkB peptide we designed did not include a linker between the TAT domain and the TrkB-FL cleavage site (Figure S3A).

neurons (DIV14) transduced with either LV-GFP (H) or LV-ICD (I) and stained with phalloidin (F-actin, dendritic spines) and a MAP2 antibody (a-MAP2, neuronal marker). Both transduced (yellow arrowheads) and neighboring untransduced neurons (blue arrowheads) were quantified. Higher-magnification insets of dendritic spines are shown in (J). (K) Quantification of dendritic protrusions in primary culture neurons (DIV14), both transduced and untransduced. Individual replicates (circles) are shown with boxplots overlaid (n = 13–15 cells, from n = 3 independent cultures per condition; two-way ANOVA followed by Šídák's test for multiple comparisons; main effects, interaction, and pairwise comparisons are shown). (L–N) Resting membrane potential (L), frequency (M), and amplitude (N) of mEPSC events recorded from primary cultured neurons transduced with either LV-GFP or LV-ICD. Individual replicates (circles) are shown with mean ± SEM (bars and error bars) overlaid (n = 7–8 cells, from n = 3 independent cultures per condition; L: t = 2.93, df = 12, $p = 1.26 \times 10^{-2}$; M: t = 2.60, df = 11, $p = 2.46 \times 10^{-2}$; N: t = 0.74, df = 11, $p = 0.47$; unpaired t tests). (O) Representative mEPSC tracings for each condition, as indicated. (P) For each GO term cataloged, the differences in the NESs for the two statistical comparisons ("TrkB-ICD overexpression" and "LV transduction") are plotted against the respective multiple-correction-adjusted p values for the TrkB-ICD overexpression contrast. Solid lines are hyperbolic thresholds (with asymptotes at an NES differential of 0.5 and an FDR of 0.05). (Q) The GO terms shortlisted in (P) are shown, with indication of their catalog ID, NES, and Benjamini-Hochberg corrected p value for the TrkB-ICD overexpression contrast. (R) Differential gene expression results represented as a volcano plot for the TrkB-ICD overexpression contrast. The horizontal dashed line represents the significance threshold of $p < 0.05$ after Benjamini-Hochberg correction for multiple testing. Each dot represents a gene; significantly upregulated genes due to TrkB-ICD overexpression are labeled in red. See also Figure S2.

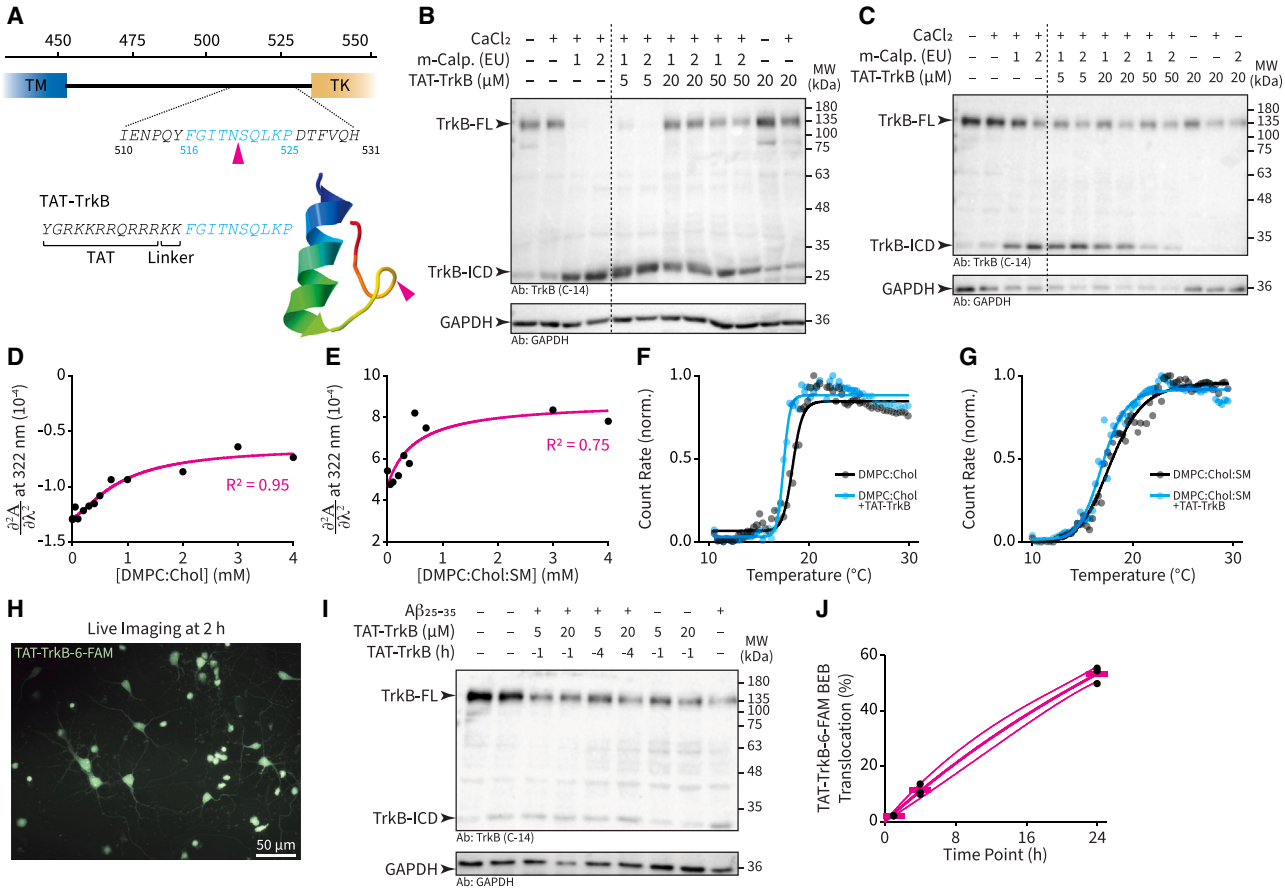

Figure 3. A TAT-TrkB peptide with a lysine-lysine linker attenuates TrkB-FL cleavage, has high affinity for cell membranes, and is readily translocated to the cytosol and across an *in vitro* model of the BEB

(A) Schematic depicting the TrkB-FL aminoacid sequence flanking calpains' cleavage site, and the design of the TAT-TrkB peptide. The predicted 3D structure of the peptide is shown (bottom right); pink triangles indicate the position of the cleavage site. (B and C) Western blots of homogenates from adult rat brain cortex (B) and primary neuronal culture (DIV8) (C). Calpain-mediated cleavage of TrkB-FL was prevented by the TAT-TrkB peptide (20 and 50 μM). (D and E) Representative experiments of TAT-TrkB partition coefficient determination in simpler DMPC:Chol (85:15) (D) and more complex DMPC:Chol:SM (75:15:10) (E) LUVs (n = 3 independent experiments). The fitted curves were obtained by applying Equation 1 to the second derivative values of the absorbance spectra at 322 nm (see materials and methods and Figure S4 for more details). (F and G) Representative experiments of T_m determination. Normalized count rate of DMPC:Chol (F) and DMPC:Chol:SM (G) LUVs (4,000 μM) with and without TAT-TrkB (4 mg/mL) are plotted as a function of temperature at pH 7.4 (n = 3 independent experiments, F: T_m = 18.4°C ± 0.5°C and T_m = 17.4°C ± 0.7°C in the absence and presence of TAT-TrkB, respectively; U = 1, p = 0.20; G: T_m = 17.7°C ± 0.4°C and T_m = 17.4°C ± 0.7°C in the absence and presence of TAT-TrkB, respectively; U = 3, p = 0.70; Mann-Whitney U tests). Fitted lines were plotted according to Equation 2 (see materials and methods). (H) Representative epifluorescence image of live primary cultured neurons (DIV14) after a 2-h incubation with TAT-TrkB-6-FAM. (I) Western blot of primary cultured neurons (DIV8). Aβ-driven cleavage of TrkB-FL was attenuated by the TAT-TrkB peptide (5 and 20 μM) incubated either 1 h or 4 h before the start of the 24 h incubation with $Aβ_{25-35}$ (25 μM). (J) Translocation kinetics of TAT-TrkB peptide through an *in vitro* model of the BEB (n = 3 independent experiments for each time point; each data point is the average of triplicates). Individual data points (black circles) are plotted, with averages (pink bars) and a hyperbolic regression with a 95% confidence interval ribbon overlaid (for schematic and BEB integrity assays, see Figure S5). See also Figures S3–S5.

We found that this peptide could not prevent TrkB-FL cleavage (Figures S3E and S3F), possibly due to its weaker propensity for α-helix conformation.[22–24] Thus, in subsequent designs, we included a linker sequence.[25] We analyzed *in silico* the three-dimensional (3D) structural conformation of peptides with different linkers (Figures 3A and S3B–S3D). The peptide that displayed the highest propensity for α-helical conformation and greater TrkB-FL cleavage site exposure included a lysine-lysine (KK) linker; thus, this peptide was analyzed in subsequent assays (henceforth called TAT-TrkB; Figure 3A).

We observed that this TAT-TrkB peptide attenuated TrkB-FL cleavage induced by recombinant calpain in protein homogenates from (1) rat brain cortex (Figure 3B) and (2) primary cultured neurons (Figure 3C). To assess the properties of this peptide in greater detail, additional *in vitro* assays were performed. Liposomes of different complexity were used to study drug-membrane interactions. We found that the TAT-TrkB peptide (1) displayed high affinity for cell membranes, particularly for more complex membranes (1,2-dimyristoyl-*sn*-glycero-3-phosphocholine:cholesterol [DMPC:Chol]: partition coefficients [K_P] = 1,275 ± 91 and logD = 3.11 ± 0.03;

DMPC:Chol:Sphingomyelin [DMPC:Chol:SM]: K_P = 4,968 ± 1,440 and logD = 3.70 ± 0.13; representative experiments are shown in Figures 3D and 3E [see materials and methods and Figure S4 for details]), and (2) did not disturb biophysical properties, namely the fluidity, of simple (DMPC:Chol) or more complex (DMPC:Chol:SM) biological membranes (representative experiments shown in Figures 3F and 3G, respectively). Furthermore, we observed that once exposed to neurons in culture, the TAT-TrkB peptide was completely internalized after only 2 h (Figure 3H) and that it attenuated Aβ-driven cleavage of TrkB-FL (Figure 3I).

Finally, using a well-established *in vitro* model of the blood-endothelial barrier (BEB),[26] a simpler model of the BBB, we confirmed that the TAT-TrkB peptide could translocate the BEB over time, reaching 53% of translocation after 24 h (Figure 3J), without compromising the integrity of the BEB (Figure S5).

TAT-TrkB prevents $A\beta_{1\text{-}42}$-induced synaptotoxicity and loss of synaptic BDNF signaling

The results above demonstrate that the TAT-TrkB peptide can reduce the cleavage of TrkB-FL, the cognate receptor of BDNF. Next, we performed electrophysiology and radioactive assays to test whether such reduction in TrkB cleavage suffices to improve synaptic transmission and plasticity under Aβ-toxic conditions.

To control for effects specific to the aggregation state of Aβ, we prepared different species of $A\beta_{1\text{-}42}$ (200 nM) (characterized by dynamic light scattering [DLS] and SDS-PAGE; Figure S6). We evaluated the effects of $A\beta_{1\text{-}42}$ species on cellular viability, dendritic spine morphology, and synaptic transmission in both primary cultured neurons (Figure S7) and hippocampal neurons *ex vivo* (Figure S8). As expected, we found $A\beta_{1\text{-}42}$ oligomers and fibrils, but not monomers, to be toxic, validating their use in subsequent experiments.

Long-term potentiation (LTP) is generally regarded as the neurophysiological correlate of cognition. To assess the induction, maintenance, and saturation kinetics of LTP, we delivered successive bouts of naturalistic θ-burst stimulation, spaced 1 h apart,[27] to hippocampal *ex vivo* slices (Figure 4A). Both oligomeric and fibrillar $A\beta_{1\text{-}42}$ species impaired LTP magnitude (Figures 4B, S9A, and S9B), but only $A\beta_{1\text{-}42}$ oligomers induced a significant desaturation of LTP, as shown by an increase in the LTP's saturation index (SI) (Figures 4C and S9C). After co-exposure to both $A\beta_{1\text{-}42}$ oligomers and TAT-TrkB (20 μM), the LTP magnitude was re-established and the saturation profile normalized ($LTP1_{Oligomers}$ = 16.04% ± 3.97%, $LTP1_{Oligomers+TAT}$ = 48.01% ± 8.71%, $SI_{Oligomers}$ = 7.43 ± 0.37, $SI_{Oligomers+TAT}$ = 4.49 ± 0.41; Figures 4A–4C). TAT-TrkB alone did not affect the excitability of hippocampal neurons (Figures S10A and S10B) or the LTP saturation profile (Figures 4B and 4C). Consistently, we found that MDL28170 (20 μM), a general calpain inhibitor, also prevented the LTP impairment and desaturation induced by oligomeric $A\beta_{1\text{-}42}$ (Figures S9D–S9F).

Next, to understand whether the ability of BDNF to modulate synaptic events in Aβ-toxic conditions was restored when TrkB-FL cleavage was attenuated by TAT-TrkB, we directly examined the effects of acutely applied exogenous BDNF. In control conditions, BDNF (30 ng/mL) potentiated both LTP magnitude (Figures 4D and 4G) and K^+-evoked glutamate release (Figures 4H and 4J), as previously shown.[16,28]

Following exposure to $A\beta_{1\text{-}42}$ enriched in oligomeric species, the effect of BDNF on LTP (Figures 4E and 4G) and glutamate release (Figures 4I and 4J) was abolished. However, following exposure to $A\beta_{1\text{-}42}$ enriched in monomeric or fibrillar species, the effects of BDNF were preserved (Figures S10D, S10E, S10H, and S10J). TAT-TrkB peptide prevented the loss of BDNF's effect on glutamate release driven by oligomeric Aβ (Figures 4I and 4J), but LTP was not potentiated further by exogenous BDNF (Figures 4F and 4G). However, co-applying TrkB-Fc, a scavenger of BDNF, reduced LTP magnitude, which means that TrkB-FL receptors were functional due to the protective effect exerted by the TAT-TrkB peptide and that endogenous BDNF signaling is necessary for maintenance of synaptic potentiation in these Aβ-toxic conditions (Figure S10G). TAT-TrkB per se did not alter the effect of BDNF (Figures 4G, 4J, S10F, and S10L).

In vivo administration of TAT-TrkB improves synaptic deficits and cognitive performance of a transgenic mouse model of AD

The results described above demonstrate that TAT-TrkB attenuates TrkB-FL receptor cleavage in Aβ-toxic conditions, which, in turn, prevents the loss of the modulatory effect of BDNF on synapses and leads to improved hippocampal plasticity *ex vivo*. To assess a possible neuroprotective effect *in vivo*, we next administered TAT-TrkB to 5XFAD mice and evaluated cognitive behavior, synaptic plasticity, and the density of dendritic spines. The 5XFAD mice express five familial AD (FAD) mutations in two genes—the human Aβ precursor protein 695 (APP695) and presenilin 1 (PS1)—and were shown to rapidly recapitulate features of AD amyloid pathology.[29]

Amyloid deposition in the brains of 5XFAD mice starts at 2 months of age, and memory deficits ensue from 4 to 5 months of age.[29,30] Therefore, we started treatment with TAT-TrkB (25 mg/kg) or NaCl 0.9% (as a control), administered intraperitoneally (i.p.), at 4 months of age, to either 5XFAD mice or wild-type (WT) littermates, for up to 9 consecutive weeks, 5 days/week (Figure 5A). Quantification of TrkB-FL and TrkB-ICD levels in the hippocampus through western blot analysis showed increased TrkB-FL cleavage in 5XFAD mice when compared to WT (Figures 5B–5D). Treatment with TAT-TrkB prevented both the reduction of TrkB-FL and the increase of TrkB-ICD in 5XFAD mice (Figures 5B–5D).

Hippocampal-dependent memory was assessed by the Morris water maze (MWM) test, in which both memory acquisition (learning phase) and retention (probe test) were evaluated. Chronic administration of TAT-TrkB prevented both learning and memory deficits in 5XFAD mice (Figures 5E–5H). During the learning phase, 5XFAD animals treated with TAT-TrkB showed decreased latency to find the escape platform, when compared with 5XFAD animals treated with vehicle (Figures 5E and 5F). TAT-TrkB treatment also reestablished the retention ability of 5XFAD mice, as observed in the probe

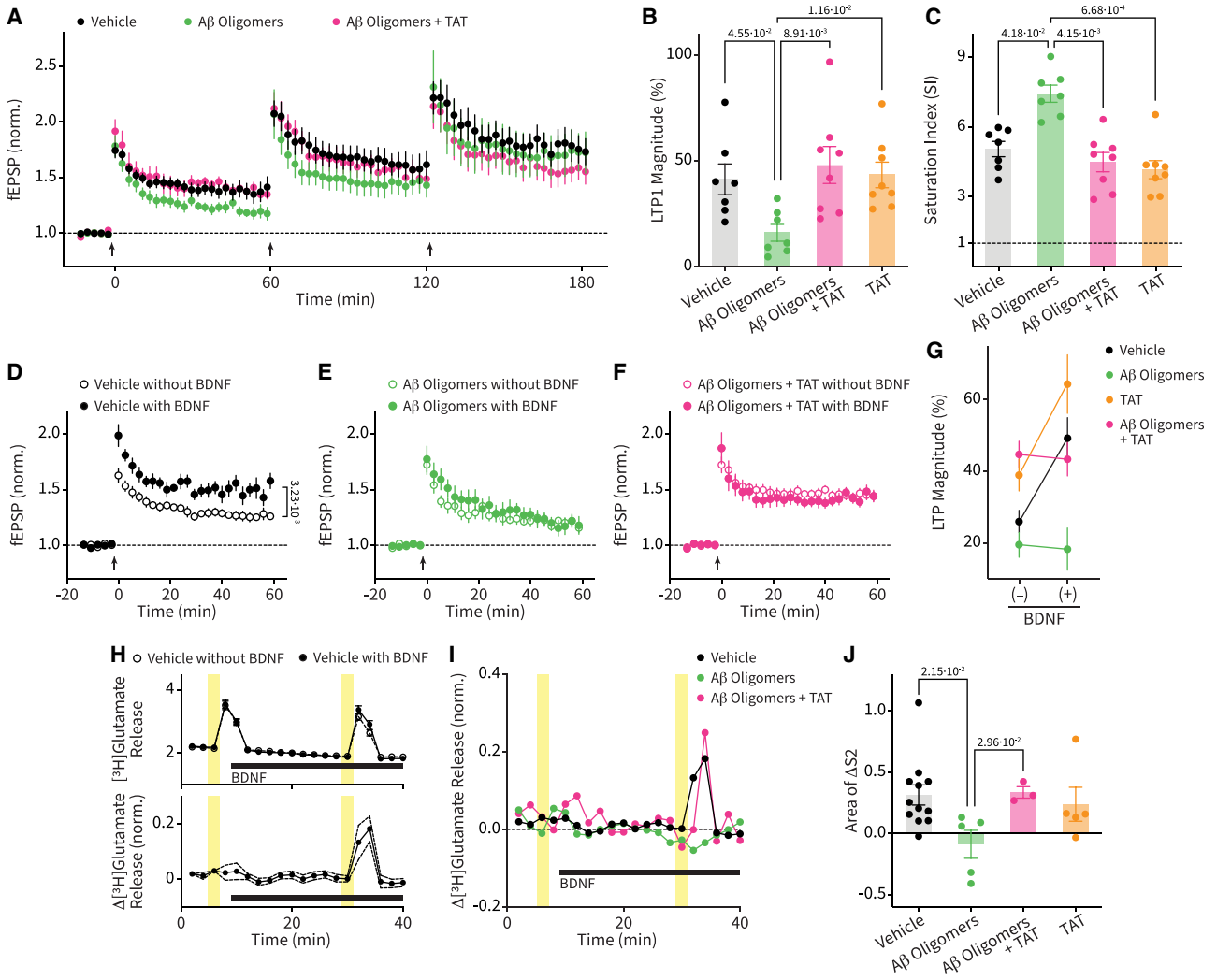

Figure 4. The TAT-TrkB peptide prevents synaptotoxic effects of Aβ_{1-42} oligomers

(A) Time course of averaged normalized changes in fEPSP slope after delivery (0, 60, and 120 min) of three weak θ-burst (4 × 4), separated by 1-h intervals, to hippocampal slices exposed to vehicle, Aβ oligomers (200 nM), or both Aβ oligomers (200 nM) and TAT-TrkB (20 μM). Data are expressed as mean ± SEM (n = 7–8 slices, from n = 7–8 rats per condition). (B and C) Quantifications of the LTP1 magnitude (B) and SI (C) from the recordings shown in (A), and from hippocampal slices exposed to TAT-TrkB (20 μM) alone (n = 8 slices, from n = 8 rats). Individual replicates (circles) are shown with mean ± SEM (bars and error bars) overlaid (B: H = 11.52, p = 9.22 × 10^{-3}; C: H = 15.77, p = 1.26 × 10^{-3}; Kruskal-Wallis test, followed by Dunn's test for multiple comparisons). (D–F) Time courses of averaged normalized changes in fEPSP slope after delivery (0 min) of a weak θ-burst (4 × 4) in the absence (colored open circles) or presence (colored filled circles) of BDNF (30 ng/mL) to hippocampal slices exposed to vehicle (D), Aβ oligomers (200 nM, E) or Aβ oligomers (200 nM) and TAT (20 μM, F). Data are expressed as mean ± SEM (D: n = 13 [no BDNF], n = 6 [with BDNF]; E: n = 8 [no BDNF], n = 7 [with BDNF]; F: n = 15 [no BDNF], n = 13 [with BDNF] slices, from different rats). (G) Quantification of LTP magnitudes from the recordings shown in (D)–(F) and in Figure S10F. BDNF significantly increased LTP magnitude after incubation with vehicle or TAT-TrkB (20 μM) alone (D: U = 7, p = 3.23 × 10^{-3}; E: U = 21, p = 0.44; F: U = 94, p = 0.89; Mann-Whitney U tests). (H) Top: time course of averaged normalized changes in fractional release of [^{3}H]glutamate from hippocampal synaptosomes, evoked by two 15-mM K^+ stimuli (at 5–7 min and 29–31 min; shaded areas), in the absence (colored open circles) or presence (colored filled circles) of BDNF (30 ng/mL). Bottom: same time course as above, where the internal control curves were subtracted from BDNF curves. This procedure makes the incremental effect of BDNF on glutamate release during the second K^+-induced depolarization more evident. (I) Time courses of averaged control-subtracted changes in fractional release of [^{3}H]glutamate from hippocampal synaptosomes induced by BDNF, after incubation with vehicle (n = 12 experiments, 24 rats), Aβ oligomers (200 nM) (n = 5 experiments, 10 rats), or both Aβ oligomers (200 nM) and TAT-TrkB (20 μM) (n = 3 experiments, 6 rats). (J) Area of control-subtracted S2 peaks from the recordings in (I) and after incubation with TAT-TrkB (20 μM) alone (n = 5 experiments, 10 rats; see Figure S10L). Individual replicates (circles) are shown with mean ± SEM (bars and error bars) overlaid (U = 9.25, p = 2.61 × 10^{-2}; Kruskal-Wallis test, followed by Dunn's test for multiple comparisons). See also Figures S6–S10.

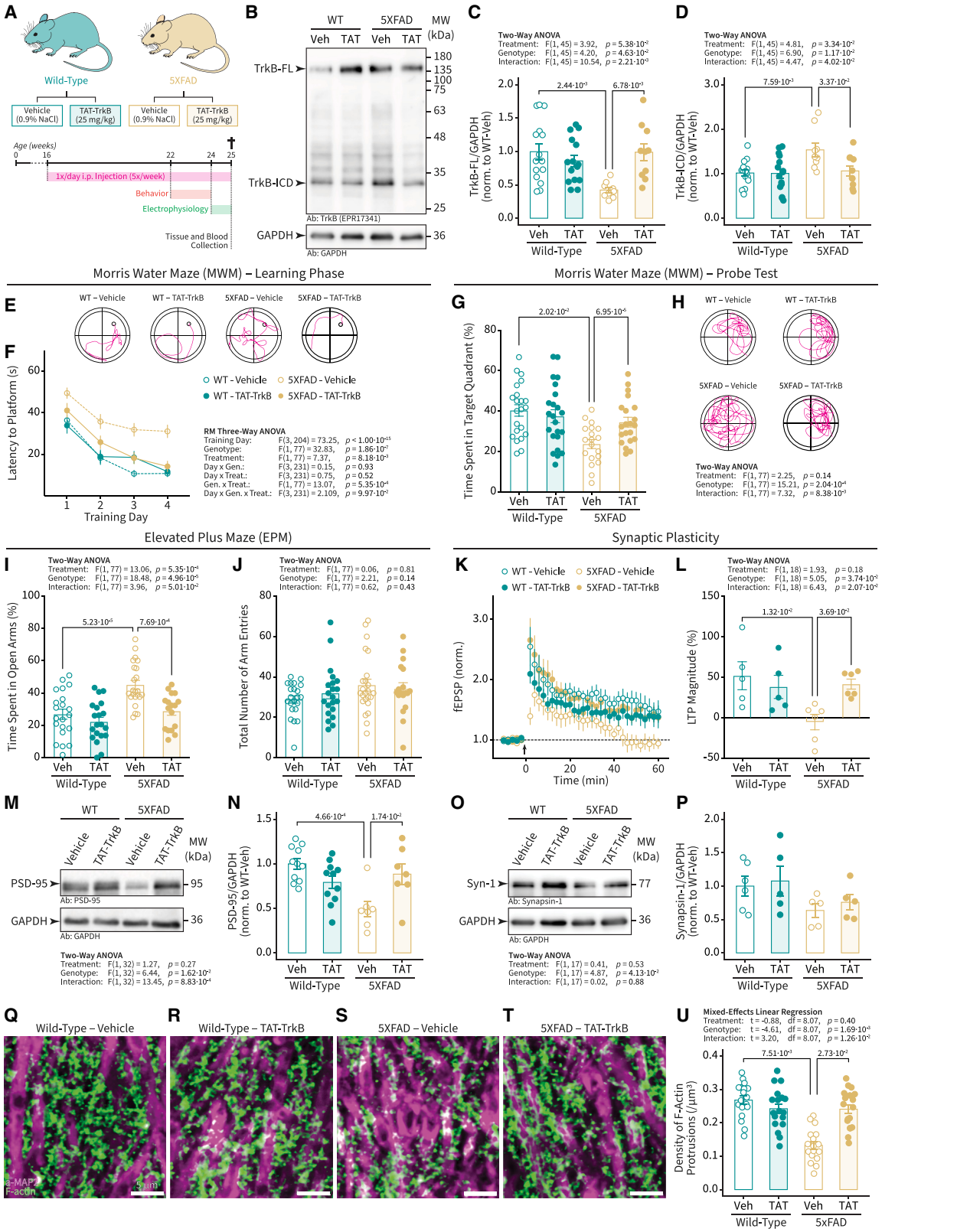

(legend on next page)

test (Figures 5G and 5H). We also evaluated an anxiety-related behavior with the elevated plus maze (EPM) test. We observed that 5XFAD mice, compared to WT, spent more time in the open arms and correspondingly less time in the closed arms (Figure 5I), with no changes in the total number of arm entries (Figure 5J), indicating decreased anxious-like behavior, as previously reported.[31,32] Importantly, similar changes in EPM performance were shown in mouse models of hippocampal neuronal loss.[33] Treatment with TAT-TrkB prevented the decreased anxious-like behavior in 5XFAD mice, while having no effect in WT mice (Figure 5I). Furthermore, TAT-TrkB had no impact on the locomotor performance of mice, regardless of their genotype, as shown by the open field (OF) test (Figure S11).

To gain a deeper mechanistic insight into the therapeutic effect of the TAT-TrkB peptide on the cognitive behavior of 5XFAD mice, we next evaluated synaptic plasticity in hippocampal slices *ex vivo*. We observed a decreased LTP magnitude in vehicle-treated 5XFAD mice compared to vehicle-treated WT controls ($LTP_{WT\ Veh}$ = 51.88% ± 17.38%, $LTP_{5XFAD\ Veh}$ = −5.440% ± 9.54%; Figures 5K and 5L), as previously reported.[34,35] LTP deficits were prevented by the chronic administration of TAT-TrkB ($LTP_{5XFAD\ Veh}$ = −5.44% ± 9.54%, $LTP_{5XFAD\ TAT}$ = 41.60% ± 6.23%; Figures 5K and 5L).

Possibly related to the impairments in synaptic plasticity, we found that vehicle-treated 5XFAD mice had decreased levels of PSD-95 (a postsynaptic protein) and of Synapsin-1 (a presynaptic protein), compared to WT littermates (Figures 5M–5P). TAT-TrkB prevented the loss of PSD-95 (Figures 5M and 5N), but not of Synapsin-1 (Figures 5O and 5P) in 5XFAD mice.

Dendritic spines harbor the postsynaptic sites of most excitatory synapses. In line with the results on the protein levels of PSD-95, we observed a loss of dendritic spines in the *stratum radiatum* of the CA1 hippocampal area of 5XFAD mice, which was also prevented by chronic administration of the TAT-TrkB peptide (Figures 5Q–5U).

Overall, these data suggest that TAT-TrkB improved the performance of 5XFAD mice in hippocampal-dependent learning/memory tasks, which could be mechanistically linked to the effects of the peptide in preventing the loss of postsynaptic sites and the synaptic plasticity deficits in the hippocampus.

In vivo administration of TAT-TrkB reduces the amount of p-Tau and the size of Aβ plaques in a transgenic mouse model of AD

To test whether the TAT-TrkB peptide could have disease-modifying properties, we next evaluated its effects on Aβ and p-Tau pathology in 5XFAD mice. 5XFAD mice are known to develop Aβ pathology, with the initial plaques developing already at 4 months of age.[31] To evaluate the effect of the TAT-TrkB peptide on this phenotype, we performed immunostainings for Aβ and quantified the number and size of Aβ plaques. Plaque pathology was absent in the entire brain of WT littermates, while being noticeable throughout the rostrocaudal axis of the brain of 5XFAD mice (Figures 6A–6D). In the hippocampus, the TAT-TrkB peptide produced a small but significant reduction in Aβ plaque area (Figure 6F), but not in plaque density (Figure 6E). In cortex, no significant changes were observed (Figures 6G and 6H; see representative images in Figure S12). To evaluate whether the TAT-TrkB peptide changed Aβ solubility, we assessed the levels of soluble Aβ in the hippocampus through western blot analysis. We found an increase in the levels of (radioimmunoprecipitation assay [RIPA])-soluble Aβ in 5XFAD mice, as expected, which was not affected by chronic administration of TAT-TrkB (Figures 6I and 6J). Taken together, these data suggest that

Figure 5. *In vivo* treatment of 5XFAD mice with TAT-TrkB attenuates TrkB-FL cleavage and prevents hippocampal-dependent memory deficits, LTP impairment, and loss of dendritic spines

(A) Schematic representation of the experimental groups and of the time line for treatments and experiments. (B) Representative western blot of hippocampal homogenates probed with anti-TrkB and anti-GAPDH antibodies. (C and D) Quantification of TrkB-FL (C) and TrkB-ICD (D) levels in hippocampal homogenates of 5XFAD and WT mice, treated with either vehicle (Veh; 0.9% NaCl) or TAT-TrkB (TAT; 25 mg/kg). Data were normalized for the vehicle-treated WT group (n = 9–15 mice per condition). Individual replicates are shown with mean ± SEM (bars and error bars) overlaid (two-way ANOVA, followed by Šídák's test for multiple comparisons; main effects, interaction, and pairwise comparisons are shown). (E–H) Hippocampal-dependent memory performance was assessed by the MWM test, in which learning/acquisition (E and F) and memory retention (G and H) were evaluated. The latency to reach the platform is plotted as a function of the training day (F) during the learning phase (n = 18–23 mice per condition; data are expressed as mean ± SEM; repeated-measures three-way ANOVA; main effects and interactions are shown). Representative traces of the mice traveling during the 4th training day are shown in (E). The time spent on the target quadrant during the probe test is shown for each experimental group in (G) (n = 18–23 mice, per condition; individual replicates are shown with mean ± SEM [bars and error bars] overlaid; two-way ANOVA, followed by Šídák's test for multiple comparisons; main effects, interaction, and pairwise comparisons are shown). Representative traces of the mice traveling during the probe test are shown in (H). (I and J) Quantification of the time spent in the open arms (I) and of the total number of entries in both open and closed arms (J) of the EPM (n = 18–23 mice, per condition). Individual replicates are shown with mean ± SEM (bars and error bars) overlaid (two-way ANOVA, followed by Šídák's test for multiple comparisons; main effects, interaction, and pairwise comparisons are shown). (K) Time course of averaged normalized changes in fEPSP slope after delivery (0 min) of a weak θ-burst (4 × 4) to hippocampal slices from mice of each experimental group (n = 5–6 mice, per condition). (L) Quantification of LTP magnitudes from the recordings shown in (K). Individual replicates are shown with mean ± SEM (bars and error bars) overlaid (two-way ANOVA, followed by Šídák's test for multiple comparisons; main effects, interaction, and pairwise comparisons are shown). (M–P) Quantification of PSD-95 (N) and Syn-1 (P) levels in hippocampal homogenates of 5XFAD and WT mice, treated with either vehicle (0.9% NaCl) or TAT-TrkB (25 mg/kg). Data were normalized for the vehicle-treated WT group (N: n = 7–11 mice per condition; P: n = 5–6 mice per condition). Individual replicates are shown with mean ± SEM (bars and error bars) overlaid (two-way ANOVA, followed by Šídák's test for multiple comparisons; main effects, interaction, and pairwise comparisons are shown). Representative immunoblots are shown in (M) and (O), respectively. (Q–U) Quantification of F-actin (dendritic) protrusion density in the *stratum radiatum* of CA1 hippocampal area (U: n = 18 imaging fields, from n = 3 mice per condition). Individual quantifications are shown with mean ± SEM (bars and error bars) overlaid (mixed-effect linear regression, followed by Tukey's test for multiple comparisons; main effects, interaction, and pairwise comparisons are shown). Representative microscopy images are shown in (Q)–(T). See also Figure S11.

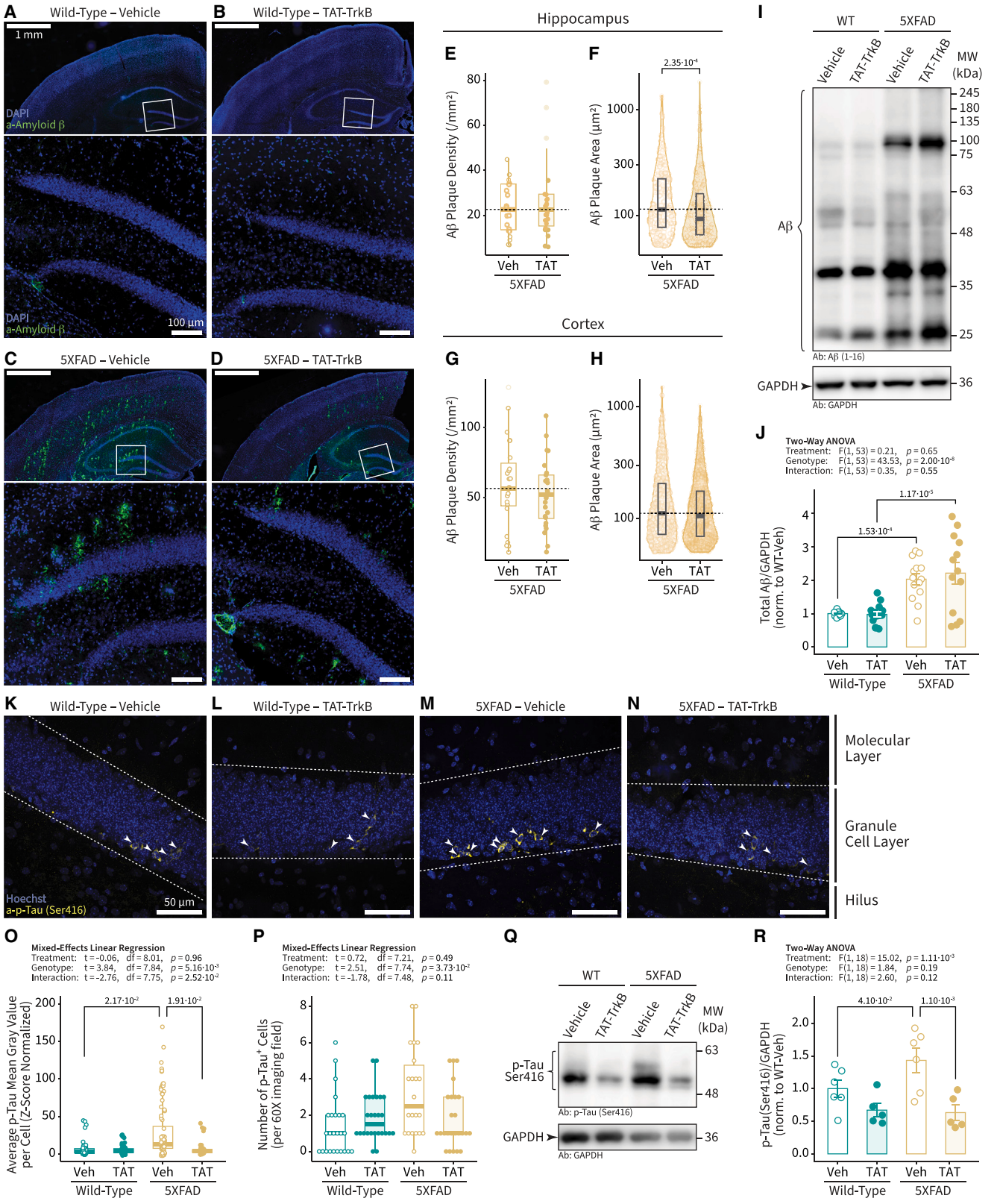

(legend on next page)

TAT-TrkB did not change the solubility of Aβ or the number of Aβ nucleation foci, although it could have slightly reduced the aggregation rate of insoluble Aβ.

Even if the 5XFAD model does not develop neurofibrillary tangles, 6-month-old mice were reported to experience significant increases in Tau phosphorylation.[36] We found p-Tau$^+$ cells in the hippocampus of both 5XFAD and WT littermates, particularly in the dentate gyrus (Figures 6K–6N). Both the number of p-Tau$^+$ cells (Figure 6P) and the mean normalized fluorescence intensity of p-Tau$^+$ cells (Figure 6O) were increased in 5XFAD mice, as compared to WT littermates. These observations suggest an increase in the expression of p-Tau in the 5XFAD model, which is consistent with previous results.[37] Although the administration of TAT-TrkB did not significantly change the number of p-Tau$^+$ cells (Figure 6P), it greatly reduced p-Tau expression levels (Figure 6O). To corroborate this finding, we performed western blot quantification of p-Tau in the hippocampus. Consistently, we found the levels of p-Tau to be increased in vehicle-treated 5XFAD mice, which was prevented by TAT-TrkB chronic administration (Figures 6Q and 6R).

These data suggest that the prevention of TrkB-FL cleavage attained by TAT-TrkB has disease-modifying properties on Tau pathology, but only minor effects on Aβ load.

Systemic administration of TAT-TrkB does not cause kidney or liver toxicity

In addition to examining the neuroprotective effects of the TAT-TrkB peptide, we aimed to perform preliminary toxicity studies, which we describe below.

Throughout the treatment period, we did not observe spontaneous deaths or clinical signs of disease in any animal undergoing treatment with TAT-TrkB (25 mg/kg). We monitored body weight as a general measurement of body condition and observed no significant changes from baseline for up to 9 consecutive weeks of treatment (Figures 7A and 7B).

Furthermore, at the end of the treatment period, a subset of animals was necropsied, the liver and kidneys were collected for histopathological analysis, and blood was harvested for biochemical measurements in the serum. We measured (1) creatine kinase (CK) to assess muscle damage; (2) creatinine and urea to determine kidney function; and (3) aspartate and alanine transaminases (AST and ALT, respectively) to evaluate liver damage. We observed no differences between groups (i.e., no effect of genotype or treatment with TAT-TrkB), and individual levels were within the ranges of reference values[38] (Figures 7C–7E, 7J, and 7K). Furthermore, no significant histological changes were detected in kidney or liver samples for either WT or 5XFAD treated with either vehicle or TAT-TrkB (25 mg/kg) (n = 3 mice per condition; representative microphotographs are shown in Figures 7F–7I and 7L–7O). Samples were analyzed by a certified pathologist, and all were graded with a score of 0 (from 0 to 4; see materials and methods for details).

Overall, we found no evidence of toxicity resulting from chronic treatment with the TAT-TrkB peptide.

DISCUSSION

Here, we demonstrate that Aβ-induced cleavage of the cognate receptor of BDNF, TrkB-FL, increases with the neuropathologic severity of AD. The BDNF/TrkB-FL system is dysregulated in AD, from very early stages, as shown by CSF samples from patients with MCI due to AD, but also when AD is fully established, as revealed by the analysis of postmortem inferior temporal cortical parenchyma samples from AD human patients. Since we lack brain parenchyma samples from non-AD patients, we cannot assess whether BDNF signaling deficits in the brain parenchyma occur from the earliest stages of AD, or whether these start only in the intermediate stages of the disease. Furthermore, we cannot ascertain

Figure 6. *In vivo* treatment of 5XFAD mice with TAT-TrkB reduced Aβ aggregation and prevented Tau hyperphosphorylation

(A–D) Representative microscopy images of Aβ plaques in the hippocampus and cortex of 6-month-old 5XFAD mice (C and D). No plaques were observed in WT littermates (A and B). Insets show the dentate gyrus in higher magnification. (E and F) Quantification of Aβ plaque density (E) and area (F) in the hippocampus of 5XFAD mice treated with either vehicle (Veh; 0.9% NaCl) or TAT-TrkB (TAT; 25 mg/kg). In (E), individual quantifications are shown with boxplots overlaid (n = 23–24 imaging fields, n = 3 mice per condition; U = 268, p = 0.87, Mann-Whitney U test). In (F), individual plaques are shown with violin plots and boxplots overlaid (n = 289–309 plaques, n = 3 mice per condition; U = 40,790, $p = 2.35 \times 10^{-4}$, Mann-Whitney U test). (G and H) Quantification of Aβ plaque density (G) and area (H) in the cortex of 5XFAD mice treated with either vehicle (0.9% NaCl) or TAT-TrkB (25 mg/kg). In (G), individual quantifications are shown with boxplots overlaid (n = 23–24 imaging fields, n = 3 mice per condition; U = 314, p = 0.42, Mann-Whitney U test). In (H), individual plaques are shown with violin plots and boxplots overlaid (n = 558–657 plaques, n = 3 mice per condition; U = 178,169, p = 0.11, Mann-Whitney U test). Representative microscopy images are shown in Figure S12. (I and J) Quantification of (RIPA-)soluble Aβ levels in hippocampal homogenates of 5XFAD and WT mice, treated with either vehicle (0.9% NaCl) or TAT-TrkB (25 mg/kg) (J). Data were normalized for the vehicle-treated WT group (n = 13–15 mice per condition). Individual replicates are shown with mean ± SEM (bars and error bars) overlaid (two-way ANOVA, followed by Šídák's test for multiple comparisons; main effects, interaction, and pairwise comparisons are shown). A representative immunoblot is shown in (I). (K–N) Representative microscopy images of p-Tau$^+$ cells in the dentate gyrus of the hippocampus of 6-month-old 5XFAD mice and WT littermates. (O and P) Quantification of average normalized p-Tau intensity (O) and of the number of pTau$^+$ cells (P) in the hippocampus of 5XFAD and WT mice, treated with either vehicle (0.9% NaCl) or TAT-TrkB (25 mg/kg). In (O), average normalized p-Tau intensities of individual p-Tau$^+$ cells are shown with boxplots overlaid (n = 70–88 cells, n = 3 mice per condition). In (P), numbers of p-Tau$^+$ cells per imaging field are depicted with boxplots overlaid (n = 22–26 imaging fields, n = 3 mice per condition). Data were analyzed with mixed-effects linear regressions, followed by Tukey's test for multiple comparisons; main effects, interaction, and pairwise comparisons are shown. (Q and R) Quantification of p-Tau levels in hippocampal homogenates of 5XFAD and WT mice, treated with either vehicle (0.9% NaCl) or TAT-TrkB (25 mg/kg) (R). Data were normalized for the vehicle-treated WT group (n = 5–6 mice per condition). Individual replicates are shown with mean ± SEM (bars and error bars) overlaid (two-way ANOVA, followed by Šídák's test for multiple comparisons; main effects, interaction, and pairwise comparisons are shown). A representative immunoblot is shown in (Q). See also Figure S12.

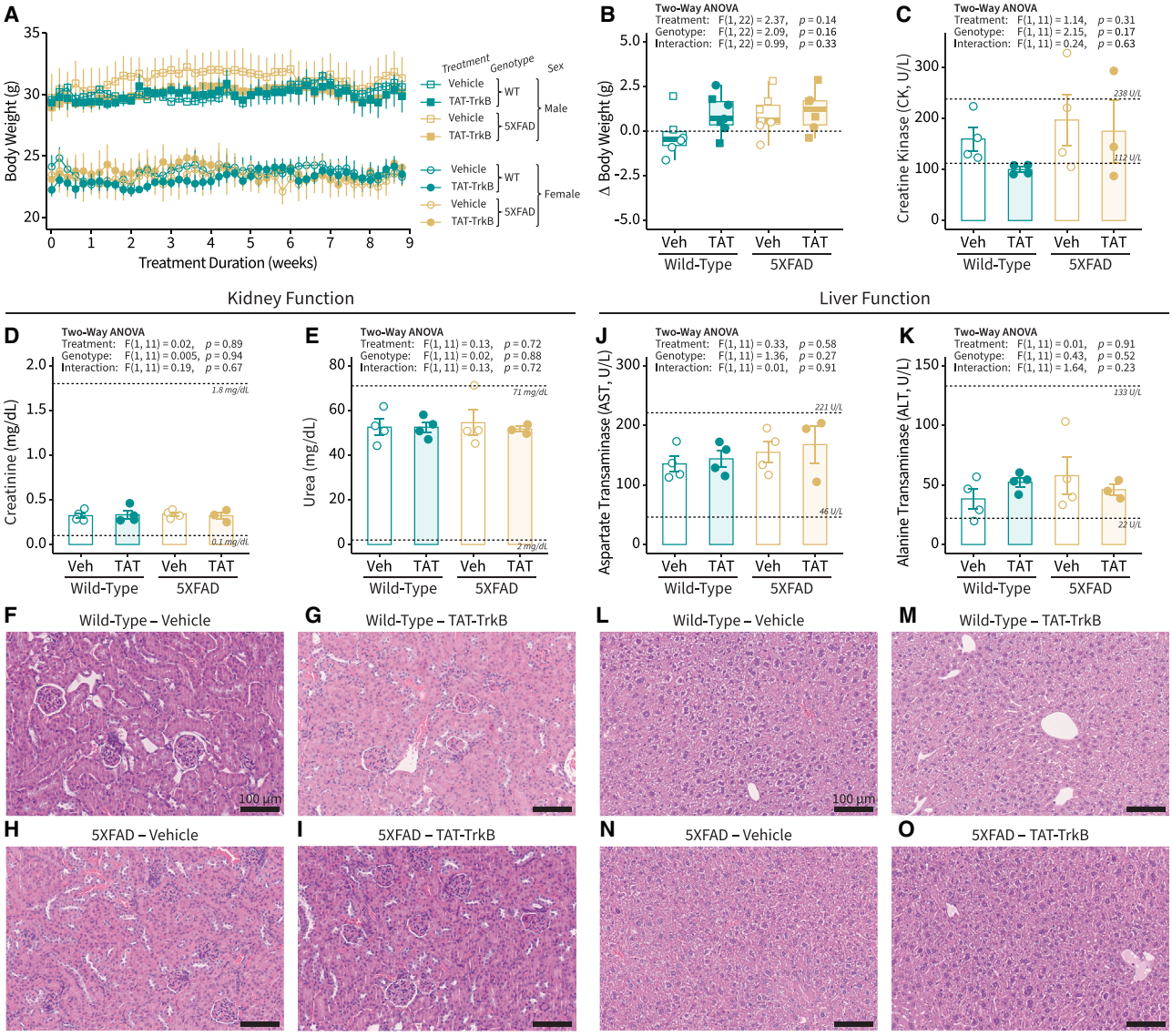

Figure 7. *In vivo* treatment with TAT-TrkB does not cause muscle, kidney, or liver damage

(A and B) Body weight is plotted as a function of experiment duration (A) (data are expressed as mean ± SEM). Changes in body weight from the start to the end of treatment are depicted in (B) (n = 6–7 mice per condition; individual replicates are shown with boxplots overlaid). (C–E) Quantification of creatine kinase (C), creatinine (D), and urea (E) in the serum of 5XFAD and WT mice, treated with either vehicle (Veh; 0.9% NaCl) or TAT-TrkB (TAT; 25 mg/kg) (n = 3–4 mice per condition; individual replicates are shown with mean ± SEM [bars and error bars] overlaid). Horizontal dashed lines indicate the range of reference values. (F–I) Representative microphotographs of H&E-stained sections of kidney. No histological changes were detected. (J and K) Quantification of AST (J) and ALT (K) in the serum of 5XFAD and WT mice, treated with either vehicle (0.9% NaCl) or TAT-TrkB (25 mg/kg) (n = 3–4 mice per condition; individual replicates are shown with mean ± SEM [bars and error bars] overlaid). Horizontal dashed lines indicate the range of reference values. (L–O) Representative microphotographs of H&E-stained sections of liver. No histological changes were detected. Analyses in (B)–(E) and (J) and (K) are two-way ANOVAs; main effects and interaction are shown.

whether TrkB-ICD formation also occurs in the hippocampus of AD patients, since we only analyzed samples from the inferior temporal cortex. Additionally, we found the levels of TrkB-ICD to be increased in CSF samples of FTD patients, suggesting that dysregulation of the BDNF/TrkB-FL system may occur across mechanistically different forms of dementia.

In this work, we assessed the potential of TrkB-FL cleavage as a pharmacological target. To this end, we designed small TAT peptides spanning the cleavage site of the receptor. We were able to validate TrkB-FL cleavage as a novel therapeutic target, since the final candidate peptide could prevent (1) TrkB-FL cleavage *in vitro* and *in vivo*; (2) Aβ synaptotoxicity *ex vivo*; and (3) synaptic plasticity deficits,

behavioral impairments, and p-Tau pathology *in vivo*. The TAT sequence increases the capacity of proteins to diffuse across the BBB,[20] obviating the need for invasive administration routes (e.g., intrathecal, intracerebral), thus facilitating the potential transition of the TAT-TrkB peptide into clinical use. Indeed, we found that the TAT-TrkB peptide could translocate an *in vitro* model of the BBB and exert effects upon the brain parenchyma *in vivo* after parenteral administration. Nevertheless, ancillary pharmacokinetic studies will be required to optimize the administration route and dosage schemes, and to fully characterize the biodistribution profile of the novel TAT-TrkB compound.

We previously mapped the cleavage site of TrkB-FL to residues N520/S521,[16] located within the juxtamembrane region of the receptor (amino acids [aa] 453–536). All TAT peptides designed in this study spanned the cleavage site (aa 516–525 or aa 513–528). Interestingly, in another study, a TAT peptide also spanning the cleavage site (aa 518–531) was shown not to protect TrkB-FL against NMDA-induced cleavage in cultured neurons.[39] The peptide in that study did not include a linker sequence, which might have compromised its conformational stability, similar to what we observed for TAT-0-TrkB in this study.

Prevention of excitotoxicity-induced cleavage of TrkB-FL was shown to increase the survival of cultured cortical neurons through phospholipase-C-γ downstream pathways and sustained activation of CREB and MEF2D.[39] However, cognitive deficits in AD precede overt neuronal loss, and even subneurotoxic concentrations of Aβ peptide can strongly suppress hippocampal synaptic plasticity.[40] Therefore, in this study, we privileged functional synaptic readouts and performance in learning/memory-related tasks. We found that the impairment of BDNF actions is sensitive to Aβ aggregation state—in other words, only oligomeric Aβ caused the loss of BDNF-induced boost in presynaptic glutamate release and postsynaptic potentiation, in line with previous evidence suggesting that oligomeric species are the most synaptotoxic.[41] Therefore, oligomeric Aβ was used in subsequent experiments to assess the neuroprotective efficacy of TAT-TrkB. TAT-TrkB prevented the loss of the effect of BDNF on presynaptic glutamate release and prevented Aβ-driven LTP impairment, but LTP could not be potentiated further by exogenous BDNF. Our first hypothesis was that, in these conditions, LTP was already saturated. To test it, we delivered successive bouts of θ-burst stimulation spaced 1 h apart.[27] Surprisingly, we found that oligomeric Aβ induced a strong LTP desaturation, a previously unknown synaptic phenotype of Aβ toxicity. We speculate that it may play a compensatory role initially, since it allows the preservation of global synaptic output despite the initial LTP impairment, but likely at the cost of excitotoxicity and eventually leads to synaptic failure and cell death. The TAT-TrkB peptide prevented the desaturation induced by Aβ oligomers, an additional mechanism whereby it may afford neuroprotection.

Soluble Aβ oligomers exert synaptotoxic effects beyond TrkB-FL cleavage, and several other receptors and pathways have been implicated.[42] Although endogenous BDNF is generally not required to sustain hippocampal LTP in juvenile animals,[43] we show here that it can be critical in Aβ-toxic conditions and that re-enabling TrkB-FL signaling with TAT-TrkB can ameliorate synaptic deficits and performance in learning/memory-related tasks.

We cannot, however, exclude that additional processing sites exist within the interdomain region that resides outside the sequence spanned by the peptide. It is challenging to target long stretches of aminoacid sequences with this strategy, since there are constraints to the size of therapeutically useful TAT peptides—specifically, toxicity increases and the ability to cross cellular membranes decreases as a function of the total peptide length.[44] Another TAT peptide spanning a different region of the juxtamembrane domain that does not include the cleavage site (aa 457–471) was found to indirectly promote TrkB-FL stability by reshuffling the recycling of the receptor to domains of the plasma membrane where it is less prone to proteolytic cleavage.[39] This peptide and the TAT peptide described here could be synergistic in protecting TrkB-FL from cleavage.

Regardless, the level of protection afforded by TAT-TrkB was sufficient to prevent the loss of BDNF effects on synaptic transmission and plasticity *ex vivo* and to prevent learning and memory deficits, synaptic impairments, and p-Tau pathology in the 5XFAD mouse model of rapidly progressing AD pathology.

The exact neuroprotective mechanism of the TAT-TrkB peptide remains unclear, and some of its effects could be cell type specific. However, the evidence presented here allows us to build a case for at least three potential mechanisms. First, TAT-TrkB prevented the Aβ-driven loss of BDNF fast synaptic actions on glutamate release and *ex vivo* hippocampal LTP; these data provide functional evidence that TAT-TrkB re-enabled TrkB-FL activation and signaling propagation through one or more of its downstream pathways. However, which pathways stay functional under the protection of TAT-TrkB remains unclear. Second, TAT-TrkB prevented the excessive accumulation of the TrkB-ICD fragment, which, by itself, as we now show, can induce dendritic spine loss and neuronal hyperactivity (both of these are also phenotypes of transgenic models of AD).[45,46] Third, TAT-TrkB prevented p-Tau pathology. Intracellular accumulation of p-Tau was shown to cause deficits in adult hippocampal neurogenesis and neural network hyperactivation, which together could be accountable for cognitive impairments.[47] In addition, several clinical studies have shown that the onset of Tau pathology is closely related to the development of cognitive symptoms.[48,49]

Even though it is generally accepted that Aβ is upstream of Tau hyperphosphorylation, how the two are linked remains a major unresolved question for the understanding of AD pathophysiology. A previous study has implicated that astrocyte reactivity could play such a role.[50] Here, we demonstrate that TrkB-FL cleavage is triggered by Aβ already in the early stages of the disease, as evidenced by our measurements in the CSF of patients with MCI due to AD. Furthermore, we found that preventing TrkB-FL cleavage also prevented the progression of Tau pathology in the 5XFAD model. Thus, it is tantalizing

to speculate that either the Aβ-driven loss of TrkB-FL receptor function or the excessive accumulation of its TrkB-ICD cleavage product could be responsible for triggering Tau phosphorylation, thereby acting as a mechanistic link between the two hallmark pathologies of AD. This hypothesis merits further research.

The therapeutic potential of TAT-TrkB may be enhanced further when combined with BDNF mimetics and/or with existing (e.g., cholinesterase inhibitors, NMDA receptor antagonist) and experimental therapies (e.g., β-secretase inhibitors, immunotherapy, plasmapheresis).[51] Furthermore, the therapeutic usefulness of TAT-TrkB may extend beyond AD, since TrkB-FL cleavage has been implicated in other diseases characterized by excitotoxic conditions, including epilepsy,[52] stroke,[53,54] and, as we now report, FTD. TrkB-FL cleavage is mediated by calpains,[16] and here we show that calpain inhibition prevents Aβ toxicity on hippocampal LTP. However, calpains serve central roles in cell physiology,[55] which greatly limits the clinical usefulness of conventional calpain inhibitors.[56]

In summary, TAT-TrkB specifically blocks a disease mechanism of AD whose therapeutic potential has not been addressed before. The *ex vivo* and *in vivo* studies conducted herein establish proof-of-concept evidence for the efficacy and safety of this therapeutic strategy. We anticipate that by preserving BDNF signaling, preventing TrkB-ICD accumulation, and decreasing Tau hyperphosphorylation, this peptide has the potential to be a disease-modifying drug that can prevent and/or reverse cognitive deficits in patients with AD.

MATERIALS AND METHODS

Human CSF samples

The CSF samples analyzed in this study are part of the "Beyond Beta Amyloid–Deciphering Early Pathogenic Changes in Alzheimer's Disease" project. The project was approved by the local ethics committee (license no. 345/18), and the participants provided their written informed consent.

Participants were recruited at Memoclínica, a private memory clinic in Lisbon, Portugal. The patient demographics are described in Table S1. The clinical history of participants was obtained at the time of CSF sampling. All patients were evaluated with a neurological examination, a comprehensive neuropsychological assessment, blood and CSF analyses, and brain imaging. The participants were in one of three groups. Group (1) were patients in the initial stages of AD, fulfilling the criteria for MCI due to AD-high likelihood, which corresponds to the highest level of diagnostic certainty as determined by National Institute on Aging/Alzheimer's Association workgroup criteria.[57] The high likelihood requires clinical and cognitive criteria, biomarkers of Aβ deposition (quantified on a CSF sample collected through lumbar puncture and based on amyloid imaging with Pittsburgh Compound-B positron emission tomography [PiB-PET]), and biomarkers of neuronal injury (in the present study, at least two had to be positive: high CSF levels of t-Tau or p-Tau, medial temporal lobe atrophy by volumetric measures or visual rating, or temporoparietal hypometabolism by [^{18}F]fluorodeoxyglucose-PET imaging). Group (2) were patients with FTD fulfilling the Rascovsky criteria for behavioral-variant FTD[58] and no biomarkers of Aβ deposition. Group (3) were subjects reporting cognitive complaints but showing none of the biomarkers of either Aβ deposition or neuronal injury indicated above (MCI controls). Patients with other neurological disorders as well as psychiatric or medical conditions that might induce cognitive deficits, history of alcohol use, or recurrent substance abuse were excluded from this study.

Lumbar puncture and CSF handling followed established standard operating protocols.[59] Upon collection, samples were clarified by centrifugation (2,000 × *g*, 10 min, room temperature), and aliquots of 500 μL were stored in code-labeled polypropylene tubes at −80°C until use.

Human brain samples

Human postmortem brain samples (from the inferior temporal cortex) were collected, and RNA and protein were extracted, as previously described.[60] The patient demographics are described in Table S2. Samples were classified according to Braak staging and grouped into three categories: stages 0–II (mild AD), stages III–IV (moderate AD), and stages V–VI (severe AD).[61] Previous quantifications of these tissue samples showed that β-secretase activity and soluble $A\beta_{1\text{-}42}$ peptide levels were correlated with the severity of AD pathology. Furthermore, the levels of $A\beta_{1\text{-}42}$, t-Tau, and p-Tau in the CSF of patients from the same series were found to be associated with disease severity, according to Braak staging.[60] Thus, these data validate the use of this cohort to assess TrkB-FL cleavage at different stages of AD pathology severity. The study was approved by the ethics committee of Kuopio University Hospital, University of Eastern Finland, the Finnish National Supervisory Authority, and the Finnish Ministry of Social Affairs and Health (license no. 362/06.01.03.01/2017).

Animals

All animal procedures were approved internally by Órgão Responsável pelo Bem-Estar Animal of Instituto de Medicina Molecular João Lobo Antunes, under license number AWB_2016_17, and externally by Direção-Geral da Alimentação e Veterinária (the Portuguese veterinary authority) under license number 002477/2021. Experiments were carried out according to the Portuguese law for animal care (Decree-Law no. 113/2013) and the European Commission guidelines for animal care (European Union Council Directive 2010/63/EU). Throughout the underlying experimental work, care was taken to minimize the number of animals sacrificed. All animals were kept under regulated temperature (22°C–24°C), relative humidity (45%–65%) and lighting conditions (14/10-h light/dark cycle), with ad libitum access to water and food.

Embryos (embryonic day [E] 17–18) from female pregnant Sprague-Dawley rats were used to prepare primary neuronal cultures, while male Wistar rats (7–10 weeks old) were used for acute hippocampal slice electrophysiology and radioactive neurotransmitter release. These animals were obtained from Charles River Laboratories (Barcelona, Spain).

In vivo and *ex vivo* studies were performed in 5XFAD transgenic mice (B6SJL-Tg(APPSwFlLon, PSEN1*M146L*L286V)6799Vas/Mmjax; The Jackson Laboratory, strain no. 034840) (16–25 weeks old). The 5XFAD mice overexpress mutant human APP695 with the Swedish (K670N, M671L), Florida (I716V), and London (V717I) FAD mutations, as well as the human PS1 gene with two FAD mutations (M146L and L286V). The expression of both transgenes is driven by the neuron-specific mouse Thy1 promoter. The 5XFAD line was maintained by crossing heterozygous transgenic mice with WT B6SJLF1/J breeders. All transgenic mice used for the experiments were heterozygotes with respect to the transgene, and non-transgenic littermates (WT) served as controls.

ELISA and western blot analyses of human CSF samples

$A\beta_{1-42}$, t-Tau, and p-Tau levels in the CSF were determined using a sandwich ELISA (INNOTEST β-AMYLOID [1–42], INNOTEST hTAU-Ag, and INNOTEST PHOSPHO-TAU 181P; Fujirebio, catalog nos. 81583, 81572, and 81574). BDNF levels in the CSF were quantified using the Human/Mouse BDNF DuoSet ELISA (R&D Systems, catalog no. DY248), according to the manufacturer's instructions.

For TrkB-ICD and TrkB-FL quantification, CSF samples were concentrated using 10-kDa filters (VWR, catalog no. 516-849). Briefly, filters were activated with 1% BSA (Sigma, catalog no. A8412) in PBS (pH 7.4) for 1 h at room temperature. Then, Milli-Q water was added, followed by centrifugation (14,000 × *g*, 10 min, 4°C). Subsequently, samples were filtered by centrifugation (14,000 × *g*, 10 min, 4°C) and the supernatant was collected. RIPA buffer containing 50 mM Tris-HCl (pH 7.5), 150 mM NaCl, 5 mM EDTA, 0.1% SDS, 1% (v/v) Triton X-100, protease inhibitors (Roche, catalog no. 11697498001), and phosphatase inhibitors (10 mM NaF and 5 mM Na_3VO_4) was added to the sample retained in the filter. The second supernatant was collected and stored together with the first supernatant. Western blot analyses were performed as described below for the human brain samples.

Transcriptomics, proteomics, and western blot analyses of human brain samples

mRNA and protein samples underwent microarray and proteomic analyses as described previously.[60] Protein extraction from frozen temporal lobe tissue samples was performed as described.[62] Protein quantification of brain lysates was performed using the Pierce BCA Protein Assay Kit (Thermo Fisher Scientific, catalog no. 23225). Total proteins (20 μg/lane) were separated by electrophoresis on NuPAGE 4%–12% bis-Tris-PAGE (Thermo Fisher Scientific, catalog no. NP0321BOX) under reducing conditions and subsequently blotted onto polyvinylidene difluoride (PVDF) membranes using the iBlot 2 Dry Blotting System (Thermo Fisher Scientific, catalog no. IB21001). After blocking with 3% BSA (Sigma, catalog no. 05482-25G) in Tris-buffered saline with Tween 20 (TBS-T; 20 mM Tris-base, 137 mM NaCl, and 0.1% Tween 20), membranes were washed three times with TBS-T, before incubation with the primary (overnight at 4°C) and secondary antibodies (1 h at room temperature). Antibodies were diluted in blocking solution. The following primary antibodies were used: rabbit polyclonal anti-TrkB (C-14), raised against the C terminus of TrkB-FL (1:1,000; Santa Cruz Biotechnology, catalog no. sc-11), and mouse monoclonal anti-β-actin (1:1,000; Abcam, catalog no. ab8226). The following secondary antibodies were used: goat anti-rabbit immunoglobulin G (IgG) horseradish peroxidase (HRP)-conjugated (1:10,000; Santa Cruz Biotechnology, catalog no. sc-2004) and goat anti-mouse IgG HRP-conjugated (1:10,000; Santa Cruz Biotechnology, catalog no. sc-2005). Protein bands were detected using enhanced chemiluminescence substrate (ECL Prime Western Blotting Detection Reagent; Cytiva, catalog no. RPN2236) and the ChemiDoc MP Imaging System (Bio-Rad, catalog no. 17001402). Band intensities were quantified using the digital densitometry tool of Fiji software.[63] In these samples, two bands were found close to the estimated molecular weight of the TrkB-ICD fragment (32 kDa).[16] We performed a careful molecular weight estimation of each band. First, we correlated the migration distance of each band front of the molecular weight ladder with their known molecular weights ($R^2 = 0.99$). Second, we used this regression line to estimate the molecular weight of the two putative TrkB-ICD bands from the migration distance of their band fronts. The lower band (labeled with an arrow in Figure 1D) had an estimated weight of 31.6 kDa. Since this was the closest to the estimated weight of 32 kDa, it was the one we used for quantifications. Importantly, TrkB-FL cleavage was found to be independent of postmortem time delay to sample collection (Figures S1Q and S1R).

TAT-TrkB peptide design and structural prediction

The final TAT-TrkB peptide (Figure 3A) contains a linker (KK) connecting (1) the transduction domain motif derived from the HIV-1 protein TAT (YGRKKRRQRRR) and (2) the TrkB-FL sequence (aa 516–525) that spans the calpain cleavage site. Several TAT-TrkB peptide sequences were simulated: final TAT-TrkB: YGRKKRRQRRRKK FGITNSQLKP; first version without a linker (TAT-0-TrkB): YGRKKR RQRRRPQYFGITNSQLKPDTF; with PP as linker: YGRKKRRQRR RPPFGITNSQLKP; with Q as linker: YGRKKRRQRRRQFGITNSQL KP; and with E as linker: YGRKKRRQRRREFGITNSQLKP (Figure S3). For BEB translocation assays and live imaging of cultured neurons, a 6-FAM fluorophore was fused to the N-terminal of the final version of the TAT-TrkB peptide. All peptides were synthesized by GenScript and prepared in sterile Milli-Q water (1 mM stock solution).

For structural predictions, ConSSert software (http://ares.tamu.edu/conSSert/)[64] and the SSPro8 tool from the Scratch server (http://scratch.proteomics.ics.uci.edu/)[65] were used. For 3D structural predictions, PEP-FOLD 3.0 software via the online server Mobyle@RPBS version 1.5.1 (http://mobyle.rpbs.univ-paris-diderot.fr/)[66] was used. After initial studies aimed to determine the peptide concentration for optimal activity, all the remaining *in vitro* and *ex vivo* experiments were performed using 20 μM, which is within the concentration range previously described for similar peptides.[23,39,67]

Primary cortical neuronal cultures

Primary neuronal cultures were prepared as routine procedure in the lab.[16,18,68] Briefly, after euthanasia of the pregnant dam, embryos

(E17–18) were rapidly removed from the uterus, and brains were dissected and placed in ice-cold Hank's balanced salt solution (HBSS) (Gibco, catalog no. 14060-073). Cerebral cortices were isolated, mechanically fragmented, and digested with 0.025% (w/v) trypsin-EDTA solution (Gibco, catalog no. 25300-062) in HBSS (Gibco, catalog no. 14180-046) for 15 min at 37°C. After digestion, cells were pelleted by centrifugation (200 × *g*, 10 min, room temperature). The supernatant was removed, and HBSS supplemented with 30% fetal bovine serum (FBS) (Gibco, catalog no. 26140-079) was added. These washing steps were repeated five times to neutralize trypsin-EDTA, and, between centrifugations, cells were resuspended by pipetting to dissociate them from the tissue. Afterward, cells were resuspended in Neurobasal medium (Gibco, catalog no. 10888022) supplemented with 0.5 mM L-glutamine (Gibco, catalog no. 25030-081), 25 mM glutamic acid (Gibco, catalog no. 35050-061), 2% B-27 supplement (Gibco, catalog no. 12587-010), and 25 U/mL penicillin/streptomycin (Gibco, catalog no. 15140-122). To obtain single cells and avoid cellular clusters or tissue fragments, the suspension was filtered with a nylon filter (Falcon 70 μM Cell Strainer; Corning, catalog no. 352350), and cell density was determined by counting cells in a 0.4% trypan blue solution (Sigma, catalog no. T8154) using a hemacytometer. Cells were plated at 6×10^4 cells per square centimeter density for western blot analysis and evaluation of MTT (Sigma, catalog no. CT01) metabolism and on coverslips at 5×10^4 cells per square centimeter density for immunocytochemistry and patch-clamp recordings. Cultures were maintained in an incubator with a humidified atmosphere of 5%/95% CO_2/O_2 at 37°C with no media change. The coverslips were previously sterilized under UV light and coated with 10 μg/mL of poly-D-lysine (Sigma, catalog no. P5407-5MG) overnight and subsequently washed three times with sterile Milli-Q water.

LV production

LV plasmid generation

The pFCK-CaMKIIα-EGFP(1.3)GW plasmid (provided by P. Osten, Max Planck Institute for Medical Research, Germany; Addgene, catalog no. 27230) is a lentiviral backbone vector harboring EGFP under the regulation of the CaMKIIα promoter. The pFCK-CaMKIIα-TrkB-ICD-IRES-ZsGreen1 plasmid was generated in two steps. First, the transgene cassette containing the TrkB-ICD sequence was PCR amplified from pcDNA3.2-ICD-V5,[18] while simultaneously adding the EcoRI and BamHI restriction sites at the 5′ and 3′ edges, respectively. The TrkB-ICD cassette was then subcloned into pLVX-IRES-ZsGreen1 (Clontech, catalog no. 632187) via the EcoRI/BamHI restriction sites. Second, from the resulting pLVX-TrkB-ICD-IRES-ZsGreen1 plasmid, the transgene cassette containing the TrkB-ICD-IRES-ZsGreen1 sequence was PCR amplified, while simultaneously adding the AgeI and EcoRI restriction sites at the 5′ and 3′ edges, respectively, and then subcloned into pFCK-CaMKIIα-EGFP(1.3) GW via the AgeI/EcoRI restriction sites.

LV production and purification

The production of VSV-G-pseudotyped LVs was performed by co-transfecting plasmid pFCK-CaMKIIα-EGFP(1.3)GW or plasmid pFCK-CaMKIIα-TrkB-ICD-IRES-ZsGreen1 with a mixture of packaging plasmids (pLP1, pLP2, and pLP/VSVG; Thermo Fisher Scientific, catalog no. K497500) into HEK293FT cells (Thermo Fisher Scientific, catalog no. R70007), cultured in 10-cm tissue culture plates, using jetPEI (Polypus Transfection, catalog no. 101000053) and following the manufacturer's recommendations. The cell transfection mixture contained a 9-μg pLP1-pLP2-pLP/VSVG plasmid mixture, 3 μg LV transgene plasmid, 24 μL jetPEI, and 200 μL of a 150-mM NaCl solution. After a 20-min incubation at room temperature, the cell transfection mixture was added to the tissue culture plate, containing 10 mL Opti-MEM medium (Thermo Fisher Scientific, catalog no. 31985062). The next day, the cell culture medium was completely replaced with 10 mL fresh Opti-MEM supplemented with 2% FBS. At 72 h post-transfection, the culture supernatant was collected, clarified by centrifugation (2,000 × *g*, 10 min, 4°C), filtered through a 0.45-μm polyethersulfone filter (Millipore, catalog no. SLHPR33RS), and concentrated using a spin filter (Amicon Ultra Centrifugal Filter, 15 mL sample volume, 100 kDa molecular weight cutoff; Millipore, catalog no. UFC910096). Viral titers (transducing units [TU]/mL) were determined by the transduction of HEK293FT cells with serial dilutions of the viral solution and colony counting after blasticidin selection and adjusted to 1.0×10^6 TU/mL. The virus solution was stored in aliquots at −80°C until use.

Lentiviral transduction of primary cortical neurons

Either LV-CaMKIIα-EGFP (LV-GFP) or LV-CaMKIIα-TrkB-ICD-IRES-ZsGreen1 (LV-ICD) was added (MOI = 1) to the culture media of primary cortical neurons at days *in vitro* (DIV)3. Cell culture medium was replaced at DIV4 and DIV7. At DIV10, cells were collected for protein and RNA extraction. At DIV14, cells were used for patch-clamp recordings or MTT assays, or they were fixed for immunocytochemistry. These procedures are described in their respective sections below.

Immunocytochemistry

Spine density count

Neuronal cultures were washed with PBS (pH 7.4) and fixed in 4% paraformaldehyde (PFA; Thermo Fisher Scientific, catalog no. 28908) in PBS (pH 7.4) for 15 min at room temperature. Cells were treated with blocking solution (3% [w/v] BSA [Sigma, catalog no. 05482-25G] in PBS with 0.1% [v/v] Triton X-100) for 1 h to block nonspecific binding. After washing, cells were incubated with the primary antibodies overnight at 4°C and subsequently washed and incubated with the secondary antibodies for 1 h at room temperature in the dark. Antibodies were diluted in blocking solution. The following primary antibodies were used: rabbit monoclonal anti-TrkB (EPR17341) (1:250; Abcam, catalog no. ab181560), chicken polyclonal anti-GFP (1:500; Antibodies Inc., catalog no. GFP-1020), and mouse monoclonal anti-microtubule-associated protein 2 (MAP2) (1:200; Sigma, catalog nos. MAB3418 and M4403). The following secondary antibodies were used: goat anti-rabbit Alexa Fluor 488 (1:200; Thermo Fisher Scientific, catalog no. A-11008), goat anti-chicken Alexa Fluor 488 (1:200; Thermo Fisher Scientific, catalog no. A-11039), goat anti-mouse Alexa Fluor 568 (1:200; Thermo Fisher

Scientific, catalog no. A-11004), and goat anti-mouse Alexa Fluor 647 (1:200; Thermo Fisher Scientific, catalog no. A-21235). Then, cells were incubated for 30 min with either Alexa Fluor 488 phalloidin (Thermo Fisher Scientific, catalog no. A12379) or Alexa Fluor 555 phalloidin (Thermo Fisher Scientific, catalog no. A34055) (1:400 in PBS [pH 7.4]), which recognize filamentous actin (F-actin). F-actin plays an important role in the constitution of the cytoskeleton of dendritic spines.[69] After washing, coverslips were mounted in Mowiol mounting solution (650 mM Mowiol 4-88 [Sigma, catalog no. 81381], 3.68 M glycerol, 0.2 M Tris-base [pH 8.0], in Milli-Q water) and imaged using either a (1) spinning disk microscope (Axio Imager M2 upright microscope, Yokogawa CSU dual camera T2 spinning disk confocal scanning unit, Visitron VS-Homogenizer on an Olympus IXplore Spin confocal spinning disk microscope system) or the (2) inverted fluorescent microscope Axiovert 135 TV (Zeiss).

TAT-TrkB cellular penetration

Mature (DIV14–16) primary neuronal cultures were incubated with TAT-TrkB-6-FAM (20 μM) and maintained in an incubator with a humidified atmosphere of 5%/95% CO_2/O_2 at 37°C for 2 h. Cells were immediately imaged with the inverted fluorescent microscope Axiovert 135 TV (Zeiss).

Propidium iodide (PI) staining

Mature (DIV14–16) primary neuronal cultures were incubated with 500 nM PI (Sigma, catalog no. 81845) and maintained in an incubator with a humidified atmosphere of 5%/95% CO_2/O_2 at 37°C for 30 min. Neuronal cultures were then washed with PBS (pH 7.4) and fixed in 4% PFA (Thermo Fisher Scientific, catalog no. 28908) in PBS (pH 7.4) for 15 min at room temperature. Cells were treated with blocking solution (3% [w/v] BSA [Sigma, catalog no. 05482] in PBS with 0.1% [v/v] Triton X-100) for 1 h to block nonspecific binding. After washing, cells were incubated overnight at 4°C with a primary mouse monoclonal anti-MAP2 antibody (1:200; Sigma, catalog no. MAB3418). Afterward, cells were washed and incubated with a goat anti-mouse Alexa Fluor 488 secondary antibody (1:200; Thermo Fisher Scientific, catalog no. A-11001) for 1 h at room temperature in the dark. Coverslips were mounted in Mowiol mounting solution and imaged using the inverted fluorescent microscope Axiovert 135 TV (Zeiss).

Western blot analysis

Primary cultured neurons and rat brain homogenates

All samples were homogenized in RIPA buffer (4% NP-40, 40 mM Tris-HCl, 1 mM EDTA, 150 mM NaCl, 0.1% SDS, 10 mM NaF, 5 mM Na_3VO_4, and protease inhibitors [Roche, catalog no. 11697498001]) and prepared with the same amount of total protein (40 μg), unless stated otherwise. A loading buffer (350 mM Tris-base [pH 6.8], 10% SDS, 30% glycerol, 600 mM DTT, 0.06% bromophenol blue) was added and the mixture was boiled at 95°C–100°C for 10 min. Next, all samples and a molecular weight size marker (NZYtech, catalog no. MB090) were loaded and separated by 10% SDS–PAGE in a standard migration buffer (25 mM Tris [pH 8.3], 192 mM glycine, 10% SDS) at a constant voltage between 80 and 120 mV. Then, proteins were transferred onto PVDF membranes (Cytiva, catalog no. 10600101), previously soaked for 5 min in methanol for wet transfer conditions (25 mM Tris-base [pH 8.3], 192 mM glycine, 10% methanol). After 90 min of transfer, membranes were stained with Ponceau S solution (Sigma, catalog no. 09276-6X1EA-F) to evaluate the protein transfer efficacy. After blocking with 5% non-fat dry milk solution in TBS-T (20 mM Tris-base [pH 7.6], 137 mM NaCl, and 0.1% Tween 20), membranes were washed three times with TBS-T before incubation with the primary (overnight, 4°C) and with the secondary antibodies (1 h, room temperature). Antibodies were diluted in blocking solution. The following primary antibodies were used: rabbit polyclonal anti-TrkB (C-14) (1:1,000; Santa Cruz Biotechnology, catalog no. sc-11), mouse monoclonal anti-p-Tyr (PY99) (1:1,000; Santa Cruz Biotechnology, catalog no. sc-7020), and mouse monoclonal anti-glyceraldehyde-3-phosphate dehydrogenase (GAPDH) (6C5) (1:5,000; Thermo Fisher Scientific, catalog no. AM4300). The following secondary antibodies were used: goat anti-rabbit IgG HRP-conjugated (1:10,000; Santa Cruz Biotechnology, catalog no. sc-2004) and goat anti-mouse IgG HRP-conjugated (1:10,000; Santa Cruz Biotechnology, catalog no. sc-2005). Finally, immunoreactivity was detected using enhanced chemiluminescence substrate (ECL Prime Western Blotting Detection Reagent; Cytiva, catalog no. RPN2236) and the ChemiDoc MP Imaging System (Bio-Rad, catalog no. 17001402). Band intensities were quantified using the digital densitometry tool of Fiji software.[63] The intensities of GAPDH bands were used as loading control.

Hippocampus of 5XFAD and WT control mice

One day after the last injection of TAT-TrkB or vehicle, mice were euthanized with an overdose of sodium pentobarbital (150 mg/kg, i.p.). The brain was quickly removed, hemisected, and the left hippocampus was dissected free in ice-cold artificial CSF (aCSF) (in millimoles: NaCl 124; KCl 3; NaH_2PO_4 1.25; $NaHCO_3$ 26; $MgSO_4$ 1; $CaCl_2$ 2; and glucose 10). Tissue samples were homogenized in RIPA buffer using a Vibracell VC250 Ultrasonic Liquid Processor (Sonics & Materials, catalog no. 303075), and protein concentrations were measured using DC Protein Reagent (Bio-Rad, catalog no. 5000112). Samples were denatured, loaded (70–150 μg) and transferred, as described above. Membrane probing with primary and secondary antibodies was also performed as described above. The following primary antibodies were used: rabbit polyclonal anti-TrkB (C-14) (1:1,000; Santa Cruz Biotechnology, catalog no. sc-11), rabbit monoclonal anti-TrkB (EPR17341) (1:10,000; Abcam, catalog no. ab181560), mouse monoclonal anti-PSD-95 (K28/43) (1:1,000; Millipore, catalog no. MABN68), rabbit polyclonal anti-Synapsin-1 (1:1,000; Abcam, catalog no. ab8), rabbit monoclonal anti-p-Tau (Ser416) (D7U2P) (1:1,000; Cell Signaling Technology, catalog no. 15013), mouse monoclonal anti-Aβ (6E10) (1:1,000; BioLegend, catalog no. SIG-39300), mouse monoclonal anti-Aβ 1–16 (W0-2) (1:500; Millipore, catalog no. SIG-39300), and mouse monoclonal anti-GAPDH (6C5) (1:5,000 in blocking solution; Thermo Fisher Scientific, catalog no. AM4300). The following secondary antibodies were used: goat anti-rabbit IgG HRP-conjugated (1:10,000; Santa

Cruz Biotechnology, catalog no. sc-2004) and goat anti-mouse IgG HRP-conjugated (1:10,000; Santa Cruz Biotechnology, catalog no. sc-2005). Finally, immunoreactivity was detected using enhanced chemiluminescence substrate (ECL Prime Western Blotting Detection Reagent; Cytiva, catalog no. RPN2236) and the ChemiDoc MP Imaging System (Bio-Rad, catalog no. 17001402) or the Amersham ImageQuant 800 Imaging System (Cytiva, catalog no. 29399483). Band intensities were quantified using the digital densitometry tool of Fiji software.[63]

MTT assay

The viability of mature (DIV14–16) primary cortical neurons was evaluated by MTT (Sigma, catalog no. CT01) metabolism. For the experiment in Figure S7C, neurons were previously incubated with either PBS (pH 7.4) (vehicle) or Aβ species for 24 h. MTT was added to the original culture medium and incubated for 3 h. After incubation, the converted die was solubilized with DMSO (Sigma, catalog no. D8418). The absorbance of the converted die was measured at 570 nm, with background subtraction at 650 nm, in a microplate reader Infinite M200 (Tecan).

mEPSC recordings

mEPSCs of isolated primary neurons (DIV14–16) were evaluated by whole-cell patch-clamp immediately after treatments, as performed routinely in the lab.[68] Briefly, cells were visualized with an upright microscope (Axioskop 2FS, Zeiss) equipped with differential interference contrast optics using a Zeiss AxioCam MRm camera and a 40× IR-Achroplan objective. For the experiments in Figures 2L–2O, $EGFP^+$/$ZsGreen1^+$ cells were identified by epifluorescence using a broad-spectrum light source (LEJ, catalog no. HXP120) and a 450–490 nm excitation, 515–565 nm emission bandpass filter set (Zeiss, catalog no. 488010-9901-000). The resting membrane potential was measured immediately upon establishing whole-cell configuration. mEPSCs recordings were performed at room temperature and in voltage-clamp mode ($V_h = -60$ mV), using an Axopatch 200B amplifier (Molecular Devices). The extracellular media was gassed aCSF, supplemented with tetrodotoxin (500 nM; Tocris, catalog no. 1078), a sodium channel blocker, and gabazine (50 μM; Sigma, catalog no. S106), a $GABA_A$ receptor antagonist. Patch pipettes (4- to 7-MΩ resistance) were filled with an internal solution containing (in millimoles): K-gluconate 125, KCl 11, $CaCl_2$ 0.1, $MgCl_2$ 2, EGTA 1, HEPES 10, MgATP 2, NaGTP 0.3, phosphocreatine 1, pH 7.3, adjusted with 1 M KOH, 280–290 mOsm. Acquired signals were filtered using a built-in 2-kHz three-pole Bessel filter, and data were digitized at 5 or 10 kHz under control of the pCLAMP 10 (Molecular Devices) software program. The junction potential was not compensated for, and offset potentials were nulled before gigaseal formation. Small voltage steps (−5 mV, 50 ms) were used to monitor the access resistance throughout the experiments. The holding current was also constantly monitored and experiments in which any of these parameters varied by more than 20% were discarded.

Analysis of mEPSC events was performed using Mini Analysis software (Synaptosoft). The event detection threshold was set at 3-fold the root mean square baseline (noise). mEPSC frequency, average amplitude, and rise and decay times were determined by analyzing 5- to 10-min recording periods per cell.

RNA extraction, library preparation, and sequencing

RNA extraction

RNA was extracted from primary cortical neurons at DIV10 using the NZY Total RNA Isolation Kit (NZYtech, catalog no. MB13402), following the manufacturer's instructions. Purified RNA samples were analyzed using a 2100 Bioanalyzer Instrument (Agilent, catalog no. G2939BA) to assess mRNA quantity and quality, as reflected by rRNA levels and integrity. Only samples with RNA integrity values >8.0 were used for library preparation.

Library preparation and sequencing

Libraries were prepared from 1 μg total RNA using the TruSeq RNA Library Prep Kit version 2 (Illumina, catalog no. RS-122-2001) and loaded on an Illumina NextSeq500 system with a 150-cycle high output kit version 2.5 (Illumina, catalog no. 20024906) using the following read lengths: 80 cycles for read 1, 8 cycles for TruSeq single index, and 80 cycles for read 2. This dataset has been deposited in GEO[70] and is accessible through GEO: GSE271487.

Analysis of bulk RNA-seq data

RNA-seq read quality was assessed with FastQC (version 0.11.9), and sequencing adapter leftovers were trimmed with BBDuk (BBMap, version 39.06). Trimmed reads were mapped with the STAR aligner (version 2.7.9),[71] using default settings, against a reference generated from the *Rattus norvegicus* genome (mRatBN7.2) and annotation (mRatBN7.2.111) and modified to include the sequences for EGFP (Addgene, catalog no. 27230), ZsGreen1 (Clontech, catalog no. 632187), and Woodchuck Hepatitis Virus Posttranscriptional Regulatory Element (WPRE) (Addgene, catalog no. 27230). Quantification of aligned reads was done by the STAR aligner while mapping using the *−quantMode GeneCounts* option, to generate gene-level raw counts for each sample. Gene body coverages were estimated using RSeQC (version 5.0.1). We obtained high-quality libraries, with >88% uniquely mapped reads for most samples and uniform gene body coverage (Figures S2D and S2E). To exclude any potential contamination, we verified that lentiviral transgenes were only expressed by the sequenced samples, according to their treatment condition (Figures S2F–S2H).

Raw count matrices were exported into R (version 4.2.3). For differential expression analysis, a mixed-effects linear model was built using the *dream* statistical framework (*variancePartition*, version 1.28.9; https://doi.org/10.18129/B9.bioc.variancePartition).[72] This framework can model both random and fixed effects. Specifically, it allowed us to control for the cell culture batch by modeling it as a random variable while performing hypothesis testing on the fixed effect (i.e., whether neurons were untransduced or transduced with LV-GFP or LV-ICD). For statistical testing, to compare the three levels of a fixed factor, two comparisons suffice. These comparisons (in statistical terms, contrasts), L1 and L2, were

$$L1 = -1 \times X_{\text{Untransduced}} + 1 \times X_{\text{LV-GFP}} + 0 \times X_{\text{LV-ICD}}$$

$$L2 = -0.5 \times X_{\text{Untransduced}} - 0.5 \times X_{\text{LV-GFP}} + 1 \times X_{\text{LV-ICD}}$$

In other words, for a given gene, the contrast L1 established the comparison between LV-GFP (control LV) and untransduced neurons. Since the expression of EGFP itself is not expected to affect the transcriptome, L1 can account for effects that result from the transduction with an LV. The contrast L2, however, attributes the positive weight to LV-ICD-transduced neurons, which overexpressed TrkB-ICD. and splits the negative weight between LV-GFP-transduced and untransduced neurons, both of which did not overexpress TrkB-ICD (Figures 2F and 2G). Therefore, we named the L1 and L2 contrasts "LV transduction" and "TrkB-ICD overexpression," respectively. More simply, these vectors of weights can be expressed as:

$$L1 = [-1, 1, 0]$$

$$L2 = [-0.5, -0.5, 1]$$

It should be noted that the inner product of L1 and L2 is null, $\langle L1, L2 \rangle = 0$, which demonstrates that the two chosen contrasts are linearly independent and, thus, statistically appropriate.[73] Briefly, after modeling the mean-variance trend, empirical Bayes moderated t statistics were computed for each gene and each contrast. *p* values were adjusted for multiple testing with the Benjamini-Hochberg procedure. An FDR <0.05 was considered statistically significant.

Gene set enrichment analysis was performed with *clusterProfiler* (version 4.6.2; https://doi.org/10.18129/B9.bioc.clusterProfiler), by ranking the genes on the t statistic from *dream* and using the mapping between gene IDs and the GO terms for Rat in *org.Rn.*e.g.,*.db* (version 3.16.0; https://doi.org/10.18129/B9.bioc.org.Rn.e.g.,.db). All graphical representations were built with *ggplot2* (version 3.5.1; 10.32614/CRAN.package.ggplot2).

Calpain *in vitro* assays and rat brain homogenate preparation

Rat cortical tissue or cultured neuronal cells were homogenized in RIPA buffer, as previously described. Homogenates were clarified by centrifugation (16,000 × *g*, 10 min, 4°C), and protein concentrations were measured using DC Protein Reagent (Bio-Rad, catalog no. 5000112). Purified rat *m*-calpain (1 or 2 enzymatic units [EU]; Calbiochem, catalog no. 208718) was incubated for 30 min at 25°C in a 100-μL final volume of RIPA buffer containing the protein homogenate (100 μg for rat brain cortex experiments and 65 μg for neuronal cultured cells), 2 mM $CaCl_2$, and either the TAT-0-TrkB or the TAT-TrkB peptide (5, 20, or 50 μM, as indicated). Enzymatic digestions were stopped by boiling samples at 95°C in the presence of denaturing SDS-sample buffer and immediately processed by western blot analysis.

Studies of biophysical interaction of TAT-TrkB with liposomes

Preparation of liposomes

Liposomes were used as *in vitro* models of human cellular membranes. Liposomes were produced by the thin film hydration method, followed by extrusion to reduce their size.[74] DMPC (MW 678; Avanti Polar Lipids, catalog no. 850345), Chol (MW 386.65; Avanti Polar Lipids, catalog no. 700100), and SM (MW 703; Avanti Polar Lipids, catalog no. 860061) were used to prepare liposomes. Briefly, DMPC:Chol and DMPC:Chol:SM were dissolved in chloroform (Sigma, catalog no. 288306) and mixed in molar ratios of 85:15 and 75:15:10, respectively. A thin lipid film was obtained after rotation under a nitrogen gas stream and overnight vacuum desiccation. The dried film was hydrated with PBS (pH 7.4) to a final concentration of 5 mM. The mixture was vortexed for 10 min to obtain multilamellar vesicles (MLVs). To reduce MLV size, the suspension was placed in a water bath sonicator (VWR Ultrasonic Cleaner, catalog no. 97043-994) at 45 kHz and 37°C for 15 min and extruded 13 times through a Nuclepore track-etched polycarbonate membrane (Whatman, catalog no. 110605) with a pore size of 100 nm at 37°C.

Partition coefficient determination

The partition coefficients (K_P) of the TAT-TrkB peptide between the lipid (DMPC:Chol and DMPC:Chol:SM) and aqueous phases (PBS, pH 7.4) were determined by derivative UV-visible spectrophotometry using a high-throughput microplate protocol.[75] The concentration of TAT-TrkB (4 mg/mL) was chosen to have an absorbance value close to 1.[76] Briefly, TAT-TrkB (4 mg/mL) was added to increasing concentrations (0–4,000 μM) of biomembranes (DMPC:Chol or DMPC:Chol:SM) in a 96-well plate (non-treated, UV-Star; Sigma, catalog no. M3812). The samples were incubated with medium agitation at 37°C for 30 min, so that the partitioned peptide reached equilibrium between the aqueous and lipid phases. The same procedure was done without TAT-TrkB as control. Absorbance spectra of liposomes in the presence and absence of TAT-TrkB were determined at 37°C, in a range between 200 and 500 nm, using a microplate reader (Synergy 2, Bio-Tek Instruments).

To obtain adjusted absorption spectra, the absorption spectra of liposomes without TAT-TrkB were subtracted from the absorption spectra in the presence of TAT-TrkB. Then, the light scattering of liposomes was removed, and the band resolution improved by determining its second derivative. The partition coefficients of TAT-TrkB were determined from the second derivative spectra at a wavelength where the light scattering of large unilamellar vesicles (LUVs) was completely removed, applying a nonlinear least-squares regression to the following equation (Equation 1) (D_T versus [L]):

$$D_T = D_W + \frac{(D_m - D_W)K_P[L]V_m}{1+K_p[L]V_m} \quad \text{(Equation 1)}$$

where D_T is the second derivative determined from the absorbance of the amount of TAT-TrkB in each phase, lipid (D_m) and aqueous (D_W); K_P represents the partition coefficient; $[L]$ represents the lipid concentration (M); V_m is the lipid molar volume calculated on the specific lipid volume (L g^{-1}), its molecular weight (g mol^{-1}), and the lipid molar ratio (V_m = 0.6186 L mol^{-1} and V_m = 0.6195 L mol^{-1} for DMPC:Chol and DMPC:Chol:SM, respectively).

Membrane fluidity studies by DLS

DLS was used to determine modifications on the membrane fluidity of LUVs induced by TAT-TrkB. This method evaluates changes in the optical properties of lipids through the variation of the mean count rate (MCR) with increasing temperature. By ensuring that the size and concentration of LUVs do not vary throughout the experiment, the variation of the MCR can be attributed to modifications in the membrane structure. Thus, we determined the temperature at which alterations on the lipid physical state occur, known as the main phase transition temperature (T_m), for DMPC:Chol and DMPC:Chol:SM in the presence and absence of TAT-TrkB, using a method previously described.[77] Briefly, TAT-TrkB (4 mg/mL) was added to DMPC:Chol or DMPC:Chol:SM vesicles (4 mM) and equilibrated at 37°C for 30 min. The MCR was collected between 10.0°C and 40.0°C, with intervals of 0.3°C, using a Zetasizer Nano ZS (Malvern Pananalytical). Vesicles in the absence of the peptide were used as a control. The normalized MCR was plotted as a function of temperature. To these results, Boltzmann regression curves were fitted to determine the T_m (Equation 2)

$$MCR = \frac{A_2 - A_1}{1+10^{B\left(1/T-1/T_m\right)}} + A_1 \quad \text{(Equation 2)}$$

where MCR represents the mean count rate; A_1 and A_2 are the MCRs of liposomes at the beginning and at the end of the experiment, respectively; B is the lipid cooperativity; T is the temperature; and T_m is the phase transition temperature.

BEB translocation and integrity assays

To evaluate the ability of the TAT-TrkB peptide to translocate the BEB, we used a well-established *in vitro* model.[26] It comprises a transwell system with an insert in which bEnd.3 [BEND3] brain endothelioma cells (American Type Culture Collection [ATCC], catalog no. CRL-2299, Lot. 59618606) were cultured for 9 days. In this model, the apical chamber replicates the blood compartment, while the basolateral chamber replicates the brain compartment (Figure S5A). For these experiments, a 6-FAM fluorophore was fused to the N-terminal of the TAT-TrkB sequence to detect the peptide by fluorescence. The TAT-TrkB-6-FAM peptide (5 μM) was diluted in DMEM (Gibco, catalog no. 21063-029) and delivered to the apical compartment. After 1, 4, and 24 h of incubation, medium from the apical and basolateral compartments of different inserts were collected and their fluorescence measured at 495 nm excitation and 517 nm emission wavelengths using a Varioskan LUX Multimode Microplate Reader (Thermo Scientific, catalog no. VL0L00D0). Peptide translocation was quantified as the fluorescence detected in the basolateral compartment normalized to the sum of the fluorescence detected in both compartments. Immediately after the TAT-TrkB-6-FAM translocation assays, *in vitro* integrity studies were performed. For these, FD4 (Sigma, catalog no. FD4-1G) was diluted in DMEM to a final absorbance below 0.1 and added to the apical compartment of the same inserts and incubated for 2 h. FD4 is a fluorescently labeled dextran with a 4-kDa molecular weight and negligible translocation when cell integrity is preserved. In parallel, FD4 was also loaded on the apical compartment of inserts with untreated cells (negative control), as well as with cells exposed to EGTA (5 mM; Millipore, catalog no. 324626). EGTA served as a positive control, since it is known to disrupt tight junctions and other cell-cell adhesions. Again, samples were collected from both compartments and their fluorescence measured at 493 nm excitation and 520 nm emission wavelengths using a Varioskan LUX Multimode Microplate Reader. FD4 basal recovery was quantified as the fluorescence detected in the basolateral compartment normalized to the sum of the fluorescence detected in both compartments. For both assays, values were obtained from triplicates of three independent experiments.

Aβ species preparation and characterization

Aβ species preparation

Aβ peptide 1–42 (1 mg/mL) (GenicBio, catalog no. A-42-T) was resuspended in PBS (pH 7.4) supplemented with 0.1% ammonia solution and adjusted to a final pH 7.2. Species separation was based on an ultrafiltration process, as previously described.[78] Briefly, monomers were immediately isolated by centrifugal ultrafiltration (Amicon Ultra 10 kDa; Millipore, catalog no. UFC901024), and the flowthrough (monomers) recovered and spectrophotometrically assayed (ε_{280} = 1,490 M^{-1} cm^{-1}). Aβ (220 μM) was allowed to oligomerize by constant shaking at 600 rpm at 37°C for 16 h (oligomers) or 5 days (fibrils). After oligomerization, samples were ultracentrifuged (40,000 × *g*, 30 min). For fibril separation, the resulting 5-day pellet (fibrils) was washed with PBS (pH 7.4) and re-ultracentrifuged twice in PBS (pH 7.4). The total fibril amount was calculated by the difference between the starting oligomerization quantity and the resulting supernatant amount (ε_{280} = 1,490 M^{-1} cm^{-1}). For oligomer separation, the 16-h ultracentrifuged supernatant was further separated in centrifugal filters (Amicon Ultra 30 kDa; Millipore, catalog no. UFC903024). The concentration of the retained fraction (oligomers >30 kDa) was spectrophotometrically quantified. All Aβ species were resuspended in PBS (pH 7.4) (vehicle).

Aβ species characterization

Aβ species (0.5 μg) were characterized by (1) SDS–PAGE in 4%–15% gradient gels (Mini-PROTEAN TGX Precast Protein Gels; Bio-Rad, catalog no. 4561083), followed by western blot (mouse monoclonal anti-Aβ antibody [6E10]; 1:1,000; BioLegend, catalog no. SIG-39300) using standard procedures, and by (2) DLS, performed as previously described.[79] Briefly, the DLS experiments were performed in a Zetasizer Nano ZS (Malvern Pananalytical), with backscattering detection at 173°, equipped with a He-Ne laser (λ = 632.8 nm), using glass cuvettes with round aperture at 25°C. Aβ species were diluted to 22 μM in Tris buffer (pH 7.4). Samples were allowed to equilibrate for 15 min at 25°C before an 8-measurement set (each set averages 10 runs, 10 s per run). Each experiment was repeated three times. Data were evaluated with the Zetasizer Nano ZS software (Malvern Pananalytical) (Figure S6).

Acute hippocampal slice preparation

Young adult (7–10 weeks old) male Wistar rats were sacrificed, under deep isoflurane anesthesia, by decapitation. The 5XFAD mice and WT littermates (24–25 weeks old) were sacrificed, under deep

isoflurane anesthesia, by cervical displacement. In either case, the brain was quickly removed, hemisected, and one or both hippocampi were dissected free within ice-cold aCSF, previously gassed with 5%/95% CO_2/O_2. Slices (400 μm thick) were cut perpendicular to the long axis of the hippocampus with a McIlwain Tissue Chopper (Campden Instruments, catalog no. TC752) and allowed to recover for at least 60 min in a resting chamber, filled with gassed aCSF, at room temperature (22°C–24ºC).

Aβ incubation procedures

For the experiments in Figures 3 and S3, primary neuronal cultures (DIV8) were incubated with $A\beta_{25-35}$ (25 μM; Bachem, catalog no. 4028357.0005) for 24 h, as previously described.[16] For the experiments in Figure S7, primary neuronal cultures (DIV14–16) were incubated with either PBS (pH 7.4) (vehicle) or one of the $A\beta_{1-42}$ (200 nM) species (monomers, oligomers, or fibrils) in supplemented Neurobasal medium for 24 h at 37°C. For the experiments in Figures 4 and S8–S10, hippocampal slices were incubated with either vehicle or $A\beta_{1-42}$ (200 nM) species (monomers, oligomers, or fibrils), in gassed aCSF, for 3 h at room temperature. We chose to perform slice incubation at room temperature to avoid neuronal damage by hypoxic injury.[80] $A\beta_{1-42}$ concentration (200 nM) was chosen according to previous studies[40,78,81,82] and based on estimates that in brain parenchyma of AD patients, Aβ is present at a concentration within the nanomolar range.[83]

Immunofluorescence

PI staining of $A\beta_{1-42}$-treated rat hippocampal slices

After treatments, hippocampal slices were incubated with 500 nM PI (Sigma, catalog no. 81845) in gassed aCSF for 30 min at room temperature and then fixed in 4% PFA (Thermo Fisher Scientific, catalog no. 28908) in PBS (pH 7.4) for 15 min at room temperature. Next, slices were dehydrated with sequential solutions of 10%, 20%, and 30% sucrose, embedded in Tissue-Tek O.C.T. (Sakura Finetek, catalog no. 4583) and stored at −80°C. Serial 20-μm-thick hippocampal sections were cut on a cryostat (Leica CM3050 S, Leica Biosystems) and mounted on SuperFrost Plus glass slides (Fisher Scientific, catalog no. 10149870). Hippocampal slices were then rehydrated and boiled three times in a 10-mM citrate buffer (pH 6.0). Afterward, slices were treated with blocking solution (3% [w/v] BSA in PBS with 0.1% [v/v] Triton X-100) for 1 h at room temperature. After washing, slices were incubated with a primary mouse monoclonal anti-NeuN [A60] antibody (1:200 in blocking solution; Millipore, catalog no. MAB377) overnight at 4°C. Slices were subsequently washed and incubated with a secondary goat anti-mouse Alexa Fluor 488 antibody (1:200 in blocking solution; Thermo Fisher Scientific, catalog no. A-11001) for 1 h at room temperature in the dark. Afterward, slices were washed, incubated with 5 μg/mL Hoechst-33258 dye (Thermo Fisher Scientific, catalog no. H3569) for 5 min, washed again, mounted in Mowiol mounting solution, and imaged on the inverted fluorescent microscope Axiovert 135 TV (Zeiss).

Staining of brain slices from 5XFAD mice

One day after the last injection of TAT-TrkB or vehicle, mice were euthanized with an overdose of sodium pentobarbital (150 mg/kg, i.p.), followed by cardiac perfusion with ice-cold PBS (pH 7.4). The brain was quickly removed and hemisected, and the right hemisphere was fixed in 4% PFA (Thermo Fisher Scientific, catalog no. 28908), in PBS (pH 7.4) for 48 h at 4°C. Subsequently, the right hemisphere was washed and embedded in sucrose in sequential steps of 15% and 30% for 48 h each at 4°C. The right hemisphere was then embedded in gelatin for cryosectioning. Serial 50-μm-thick brain sections were cut on a cryostat (Leica CM3050 S, Leica Biosystems) and mounted on SuperFrost Plus glass slides (Fisher Scientific, catalog no. 10149870). Slices were first washed in TBS at 37°C to remove the gelatin, briefly post-fixed in 4% PFA (10 min, room temperature), and subsequently washed in TBS (3 × 5 min). Next, the tissue was permeabilized (0.25% Triton X-100 in TBS [pH 7.4]) for 10 min and incubated with blocking solution (5% BSA, 5% FBS, and 0.1% Triton X-100 in TBS [pH 7.4]) for 1 h at room temperature. Afterward, slices were incubated with the primary (overnight at 4°C) and secondary antibodies (2 h at room temperature), with washing steps in between (TBS, 3 × 5 min). Antibodies were diluted in blocking solution. The following primary antibodies were used: mouse monoclonal anti-Aβ (W0-2) (1:500; Millipore, catalog no. MABN10), rabbit monoclonal anti-p-Tau (Ser416) (D7U2P) (1:250; Cell Signaling Technology, catalog no. 15013), and rabbit polyclonal anti-MAP2 (1:200; Abcam, catalog no. ab32454). The following secondary antibodies were used: goat anti-mouse Alexa Fluor 568 (1:500; Thermo Fisher Scientific, catalog no. A-11004), goat anti-rabbit Alexa Fluor 568 (1:200; Thermo Fisher Scientific, catalog no. A-11011), and goat anti-rabbit Alexa Fluor 647 (1:500; Thermo Fisher Scientific, catalog no. A-21245). Simultaneously with the secondary antibodies, samples were incubated with DAPI (1:1,000; Thermo Fisher Scientific, catalog no. D1306) and, for the experiments in Figures 5Q–5U, with Phalloidin-iFluor 488 Reagent (1:500; Abcam, catalog no. ab176753). Slides were then washed once more in TBS (3 × 5 min) and mounted with Fluoromount-G mounting medium (SouthernBiotech, catalog no. 0100-01). Slides were imaged with a spinning disk microscope (Axio Imager M2 upright microscope, Yokogawa CSU dual camera T2 spinning disk confocal scanning unit, Visitron VS-Homogenizer on an Olympus IXplore Spin confocal spinning disk microscope system), using 20× (Olympus, catalog no. UPlanXApo20X) and 60× (Olympus, catalog no. UPlanSApo60X) objectives and up to three excitation laser lines, according to secondary antibody specifications.

Analysis of imaging data

For each group of experiments, all images were acquired in the same imaging session using the same laser power and exposure time. All representative images are shown with equalized brightness and contrast. All the analyses described below were performed in Fiji.[63]

Quantification of co-expression

For the experiments in Figures 2B–2E, six fields were randomly selected for each sample and imaged with a 20× objective. $EGFP^+$/$TrkB^+$ and $MAP2^+$ cells were manually counted. The ratio of $MAP2^+$ cells expressing EGFP (and vice versa) was determined for each image and averaged across images of the same sample.

For the experiments in Figures S7A–S7C, six fields were randomly selected for each sample and imaged with a 20× objective. $MAP2^+$ and PI^+ cells were manually counted. Neuronal death was expressed as the ratio of PI^+ cells among all $MAP2^+$ cells. Values were averaged across images of the same sample.

For the experiments in Figures S8A–S8E, each sample was imaged with a 4× objective, encompassing most of the hippocampus. Subfields in the CA1 and CA3 areas were analyzed. $MAP2^+$ and PI^+ cells were manually counted. Neuronal death and overall cell death were expressed as the ratio of PI^+ cells among all $MAP2^+$ cells and among all cells (identified by nuclear staining with Hoechst), respectively.

Spine density

For the experiments in Figures 2H–2K, S7D, and S7E, 8–10 fields were randomly selected for each sample and imaged with a 60× objective. Spine density was quantified as the number of small protrusions (either mushroom-shape spines or filopodia) extending $\leq$3 μm from their parent dendrite, with a distance >25 μm from the cell body, normalized to 10 μm of the parent dendrite, as previously reported.[84] Protrusions from three different dendrites per neuron were analyzed and manually quantified.

For the experiments in Figures 5Q–5U, three fields across the *stratum radiatum* of the hippocampal CA1 area were imaged with a 60× objective for each sample. For each imaging field, two smaller square subfields of 25 × 25 μm were randomly selected. F-actin protrusions (either mushroom-shape spines or filopodia) were manually counted in each subfield on a single optical section.

Aβ plaque number and size

For each sample, four fields were imaged with a 20× objective across different regions of the hippocampus and cortex each. Z stacks (step size: 0.57 μm) spanning the entire thickness of the slice at each location were flattened onto a maximum intensity projection. Flattened images were thresholded and binarized using the Otsu method to segment and define the region of interest (ROI) for each plaque. Segmented ROIs with small areas (<50 μm^2) were discarded, as they likely did not correspond to Aβ plaques. The number and area of each plaque were quantified for each image. In the hippocampus, we analyzed 289–309 plaques, from n = 3 mice, per condition. In cortex, we analyzed 558–657 plaques, from n = 3 mice, per condition.

p-Tau expression levels

For each sample, six fields were imaged, with a 60× objective, across different regions of the hippocampus. Z stacks (step size: 0.26 μm) spanning the entire thickness of the slice at each location were flattened onto a maximum intensity projection. A circular/ellipsoid ROI was manually centered on each p-Tau^+ cell on the imaging field, as well as on 10 p-Tau^- cells. We analyzed 309–340 ROIs, from n = 3 mice, per condition. After background subtraction, the average gray value of each ROI was Z score normalized for the value distribution of the p-Tau^- cells within each image. This was performed to control for most sources of technical variability in intensity values across samples and, thus, to make values comparable across different images. For the analysis in Figure 6P, a cell was considered p-Tau^+ if its average Z score normalized intensity was >3.

Extracellular ex vivo *recordings*

Slices were transferred to a submerging chamber (1 mL) and continuously superfused at a 3-mL/min rate, with gassed aCSF at 32°C. Perfusion tubes were coated with 0.1 mg/mL BSA prior to BDNF experiments to avoid BDNF adsorption to the tubes.[85] Evoked field excitatory postsynaptic potentials (fEPSPs) were recorded extracellularly through a microelectrode filled with 4 M NaCl (2- to 8-MΩ resistance) placed in the *stratum radiatum* of the CA1 area, as previously described.[68,85] One pathway of the Schaffer collateral/commissural fibers was stimulated (rectangular pulses of 0.1-ms duration) every 15 s (for input/output [I/O] curves and paired-pulse facilitation [PPF] recordings) or every 20 s (for LTP recordings) by a bipolar concentric wire electrode placed on the Schaffer fibers in the *stratum radiatum* in the CA1 area. The initial intensity of the stimulus was adjusted to obtain a submaximal fEPSP slope with a minimum population spike contamination near one-fifth of the fEPSP slope obtained with supramaximal stimulation. Averages of eight (Wistar rats) or six (5XFAD mice and WT littermates) consecutive fEPSPs were obtained, and the slope of the initial phase of the potential was quantified. Recordings were obtained with an Axoclamp 2B amplifier (Axon Instruments), digitized, and continuously stored on a computer with WinLTP software.[86] All the protocols detailed below were started only after a stable baseline of at least 20 min.

I/O curves

The stimulus delivered to the slice was decreased until no fEPSP was evoked and subsequently increased by increments of 20 μA. Data from three consecutive averaged fEPSPs were collected for each stimulation intensity. The range of inputs delivered to slices typically ranged from 60 μA to a supramaximal stimulation of 400 μA.

LTP induction and saturation

A weak LTP-inducing θ-burst protocol consisting of 4 trains of 100 Hz, 4 stimuli, separated by 200 ms was used (4 × 4).[68] The intensity of the stimulus was never changed.

For the experiments in Figures 4A–4C and S9, to test LTP saturation, three consecutive θ-burst (4 × 4) paradigms were induced in the same pathway spaced by 1-h intervals. This experimental design was based on previous results showing that LTP has a refractory period of 60 min before which a new LTP cannot be effectively induced.[27] TAT-TrkB (20 μM) or MDL28170 (20 μM; Tocris, catalog no. 1146) was used in a subset of the experiments.

For the experiments in Figures 4D–4G and S10D–S10F, BDNF (30 ng/mL; provided by Regeneron Pharmaceuticals) was added to the superfusing solution (aCSF) 20 min before the induction of LTP. Controls for these experiments were performed in different

slices without BDNF superfusion on the same day. Generally, when testing the effect of BDNF on synaptic plasticity, two independent pathways of the same hippocampal slice are used, one serving as test and the other as internal control.[28,85] However, given that, in the present experimental design, slices were previously exposed to Aβ species or PBS (pH 7.4) (vehicle) for 3 h, we chose to test the effect of BDNF in different slices from the same rats. Otherwise, the time between the end of Aβ pre-treatment and LTP induction would have been consistently longer when testing BDNF, since BDNF could only have been added to the superfusing solution after LTP was induced in the first pathway.

For the experiments in Figure S10G, TrkB-Fc (2 μg/mL; R&D Systems, catalog no. 688-TK-100), a BDNF scavenger, was added to the superfusion solution 30 min before the induction of LTP and remained in circulation up until the end of the experiment.

PPF recordings

PPF was quantified as the ratio between the second versus the first fEPSP slope (fEPSP2/fEPSP1) responses at different interstimulus intervals (10–150 ms).[68]

Analysis of extracellular recordings

For I/O curves, maximum slope values were obtained by extrapolation upon nonlinear fitting. Whenever the stimulus was intense enough to elicit a population spike (depolarization that follows the fEPSP), its amplitude was measured. Each population spike amplitude replicate was plotted as a function of the slope of the associated fEPSP, and the popspike/fEPSP ratio was calculated as the quotient between these values.[68]

LTP magnitude was quantified as the normalized change in the average slope of the fEPSPs 50–60 min after LTP induction, relatively to the average slope of the fEPSPs measured during the 10 min that preceded the induction. The LTP saturation index (SI) was calculated as the quotient of the sum of the three LTP magnitudes by the magnitude of the first LTP ([LTP1+LTP2+LTP3]/LTP1; hence, if SI ≈ 3, then LTP is fully saturated; if SI >3, then LTP is not saturated; the higher the SI, the more desaturated the LTP).

[^{3}H]Glutamate release assays

Synaptosome isolation

The synaptosomal fraction from rat hippocampi was prepared as routinely performed in the lab.[16,87] Hippocampal slices (from 7- to 10-week-old male Wistar rats) were prepared and treated with PBS (pH 7.4) (vehicle) or $A\beta_{1\text{-}42}$, as described above. Slices were then added to a 5-mL ice-cold isosmotic sucrose solution (0.32 M, containing 1 mM EDTA, 1 mg/mL BSA, 10 mM HEPES, pH 7.4) and homogenized (four up-and-down strokes) in a Potter-Elvehjem homogenizer with a polytetrafluoroethylene pestle (Corning, catalog no. 7725T-17) and the volume completed to 10 mL with an isosmotic sucrose solution. After a first centrifugation (3,000 × *g*, 10 min, 4°C), the supernatant was collected and centrifuged again (14,000 × *g*, 12 min, 4°C). The pellet was then resuspended in 1 mL 45% Percoll (Sigma, catalog no. P1644) in KHR solution (consisting of NaCl 140 mM, EDTA 1 mM, HEPES 10 mM, KCl 5 mM, and glucose 5 mM), and centrifuged (16,000 × *g*, 2 min, 4°C). The synaptosomal fraction, corresponding to the top buoyant layer, was collected from the tube. Percoll was removed by two washes with 1 mL KHR solution with a centrifugation step in between (16,000 × *g*, 2 min, 4°C). Synaptosomes were then kept on ice and used within 3 h. The synaptosomal protein concentration was assayed using DC Protein Reagent (Bio-Rad, catalog no. 5000112).

[^{3}H]Glutamate release from hippocampal synaptosomes

[^{3}H]Glutamate (L-[3,4-^{3}H]-glutamic acid; PerkinElmer, catalog no. NET490250UC) release from hippocampal synaptosomes was performed as routine procedure in the lab.[16,87] Briefly, synaptosomes (protein concentration 1–2 mg/mL) were resuspended in oxygenated aCSF solution and allowed to equilibrate for 5 min at 37°C. From that moment onward, all solutions applied to the synaptosomes were kept at 37°C and continuously gassed with 5%/95% CO_2/O_2. Synaptosomes were loaded with 0.2 μM [^{3}H]glutamate (specific activity 30–60 Ci/mmol) for 5 min and equally layered over Whatman GF/C filters (Merck, catalog no. WHA1822024) onto an eight-chamber superfusion apparatus (flow rate, 0.6 mL/min; chamber volume, 90 μL). The constant and rapid flow rate washes out endogenously related substances, thus ensuring drug specificity.[88] After a 20-min washout period, the effluent was collected for 40 min in 2-min intervals. Glutamate release from synaptosomes was elicited for 2 min using a high-K^+ solution (15 mM, isomolar substitution of Na^+ by K^+ in the perfusion buffer) at the 5th (first stimulation period [S1]) and 29th (second stimulation period [S2]) min after starting the sample collection. BDNF (30 ng/mL; provided by Regeneron Pharmaceuticals) was added to the superfusion medium at the 9th min (before S2) and remained in circulation until the end of the experiments (as indicated by the horizontal bars in Figures 4H, 4I, and S10H–S10M). Control curves, in the absence of BDNF, were performed in parallel within the same synaptosomal batch. Each condition was tested in duplicate. Hence, in each experiment, two synaptosome-loaded chambers were used as control chambers, the others being used as test chambers. Each one of the chambers was used as control or as one of the test conditions on different days. At the end of each experiment, aliquots (500 μL) of each sample and the filters from each superfusion chamber were analyzed by liquid scintillation counting.

Calculation of the effect of BDNF on glutamate release

The fractional release was expressed as the percentage of total radioactivity present in the synaptosomes at each time point. To quantify the effect of BDNF, internal control curves (performed in parallel within the same synaptosomal batch) were subtracted from BDNF curves. The incremental release induced by BDNF was quantified by integration of the area of the S2 peak upon subtraction of the estimated basal tritium release.

Intraperitoneal administration of TAT-TrkB

The TAT-TrkB peptide (25 mg/kg) was diluted in saline solution (0.9% NaCl) and administered i.p., starting at 4 months of age, to

either 5XFAD mice or WT littermates, for up to 9 consecutive weeks, 5 days/week (Figure 5A). Both the TAT-fused peptide dosage[20,89–91] and the duration of the treatment regime[89,92,93] were based on previous studies. The peptide could not be administered via an enteric route, as TAT-TrkB was not in a formulation that would have been resistant to gastric enzymes and acidity.

Heterozygous transgenic (5XFAD) mice and WT littermates were each randomly allocated to a treatment regime, dividing them into four groups: WT mice receiving either vehicle (0.9% NaCl) or TAT-TrkB (25 mg/kg) injections, and 5XFAD mice receiving either vehicle (0.9% NaCl) or TAT-TrkB (25 mg/kg) injections (Figure 5A). Behavioral assessments started on the 6th week of treatment (22 weeks old) and ended 2 weeks later, on the 8th week of treatment (24 weeks old). One day after the last injection, animals were euthanized to collect one or more of the following: (1) the left hippocampus, for western blot analysis; (2) the right brain hemisphere, for immunofluorescence stainings; (3) the kidneys and liver, for histopathological analysis; and (4) blood, for clinical chemistry. In some cases, the left hippocampus was used for electrophysiological recordings instead. Recordings started on the 8th week of treatment (24th week) and lasted 1 week.

Behavioral assessments

All behavioral tests were performed during the light phase between 8 a.m. and 6 p.m. in a sound-attenuated room. Behavioral assays were performed in the following sequence: OF test, EPM test, and, lastly, MWM test. Experimenters were blinded to animal genotype and treatment group for the duration of the behavioral testing. Mazes were cleaned with a 30% EtOH solution between each animal.

Open Field test

The OF test was used to assess locomotor and anxiety-like behavior with the objective of detecting biases in animal behavior that could affect performance in other behavioral tests. The OF test was conducted in a wood open field arena (40 × 40 × 40 cm).[94,95] This test was carried out during the first 10 min that animals had contact with this environment (i.e., without a training or habituation phase). The arena was virtually divided into three concentric squared zones: a peripheral zone, an intermediate zone, and a central zone (Figure S11A).

Mice movements were recorded and analyzed using SMART video-tracking software (version 2.5, Panlab, Harvard Apparatus Spain). The reference point used by the software to determine the position of the animal was the center of the mouse's dorsum. The total distance traveled and the average speed were quantified to compare locomotor ability. Also, the percentage of time spent in the central zone was used as an inverse indicator of an anxiety-like behavior. Lighting conditions, physical apparatus, environmental clues, and animal manipulation procedures were kept as similar as possible between animals.

Elevated Plus Maze test

The EPM maze is shaped like a plus sign and consists of two open arms (no walls, 5 × 29 cm) and two closed arms (5 × 29 × 15 cm), arranged perpendicularly, and elevated 50 cm above the floor. Each animal was placed at the center of the maze, facing an open arm, with each test lasting 5 min.

Mice movements were recorded and analyzed using SMART video-tracking software. The (1) total time spent in the open arms and the (2) total number of arm entries (i.e., sum of the number of entries in both open and closed arms) were used as anxiety-like and locomotor parameters, as previously described.[96]

Morris Water Maze test

Spatial memory was evaluated with the MWM test.[97] The test was performed over the course of 6 consecutive days and consisted of a 1-day habituation phase, a 4-day acquisition phase, and a 1-day probe test. The test was performed in a circular pool (100 cm diameter, 60 cm height), filled with water opacified with non-toxic white paint (Luxens) and kept at 24°C. A round 8-cm-diameter platform was used as an escape platform. Four positions around the edge of the tank were used, and the tank was virtually divided into four quadrants: target quadrant (T, where the platform was hidden), left quadrant (L, left of the target quadrant), right quadrant (R, right of the target quadrant) and opposite quadrant (O, on the opposite side of the target quadrant).

During habituation, each animal was familiarized with the presence of an escape platform—in this instance, placed in the center of the tank, 1 cm above water level. Animals were placed in the platform and after 20 s, they were placed back in their home cages beneath heat lamps. If the animals failed to stay on the platform for 20 s and did not climb back after 2 min, then they were guided to it and allowed to stay for an additional 20 s. Animals had a second habituation period later in the same day, with the escape platform still placed in the center of the tank, but at 1 cm below water level.

During the acquisition phase, the escape platform was submerged 1 cm below water level in a fixed position, randomized for each animal, in the center of the target quadrant. Furthermore, visual cues of different shapes and colors were placed on the walls of the testing room. Each mouse was given four swimming trials per day (with 30-min intervals between trials). A trial consisted of placing the animal in the pool facing the wall and allowing it to explore and reach the hidden platform. Each animal was released from a different and randomized quadrant (different from the one holding the escape platform) in each trial of the same day. If the animal reached the platform before 60 s, then it was allowed to remain there for an additional 10-s period; if the animal failed to find the target within that time frame, then it was manually guided to the platform, where it was allowed to remain for an additional 20 s. After the end of each trial, mice were removed from the pool and placed back in their home cages beneath heat lamps to prevent temperature loss.

During the probe test, the escape platform was removed, and animals were allowed to swim freely for 60 s while recording the percentage of time spent on each quadrant.

Mice movements were recorded and analyzed using SMART video-tracking software. The latency to find the platform during the acquisition phase and the percentage of time spent in the target quadrant in the probe test were quantified and used to evaluate hippocampal-dependent memory.

Kidney and liver histopathology

One day after the last injection of TAT-TrkB or vehicle, mice were euthanized with an overdose of sodium pentobarbital (150 mg/kg, i.p.). For each mouse analyzed, a comprehensive necropsy was performed and macroscopic findings were recorded. Kidneys and liver were harvested for histopathologic evaluation. Samples were immersion-fixed overnight in 10% neutral buffered formalin (Bio-Optica, catalog no. 05-K01009). Tissue was processed using a HistoCore PEARL Tissue Processor (Leica) and embedded into paraffin blocks using a tissue embedding station (Leica, catalog no. EG1150H). Slices, 3 μm thick, were cut using a rotary microtome (Leica, catalog no. RM2245), adhered to slides, incubated in an oven for 1 h at 60°C, and stored at room temperature until further processing.

Slices were deparaffinized and rehydrated using an Autostainer XL (Leica, catalog no. ST5010) by subsequently immersing them in the following solutions: xylene, 10 min; EtOH 100%, 5 min; EtOH 96%, 5 min; and distilled water, 5 min. Rehydrated slices were then stained with hematoxylin (Bio-Optica, catalog no. 05-06004E) and eosin (Sigma, catalog no. HT110132). Briefly, slices were treated with (1) hematoxylin, 3 min, and then rinsed with distilled water, 1 min; (2) 0.5% ammonia water, 10 s, and then rinsed with distilled water, 1 min; (3) EtOH 96%, 30 s; and finally, (4) Eosin Y solution, 10 min. Afterward, slices were dehydrated with one change of EtOH 96% and two changes of 100% EtOH, 2 min each. Finally, slides were coverslipped using Entellan mounting medium (Sigma, catalog no. 1.00869) and an automated glass coverslipper (Leica, catalog no. CV5030). Microphotographs were obtained with a Hamamatsu NanoZoomer-SQ slide scanner (Hamamatsu, catalog no. C13140), using NDP.view 2 viewing software (Hamamatsu).

The microphotographs were evaluated by a certified pathologist and lesions were classified according to a 5-tier severity scale: 0, absent; 1, minimal; 2, mild; 3, moderate; and 4, marked.[98]

Blood collection and clinical chemistry

One day after the last injection of TAT-TrkB or vehicle, mice were euthanized with an overdose of sodium pentobarbital (150 mg/kg, i.p.). Blood was harvested through cardiac puncture and up to 500 μL was collected onto gel clot activator tubes (Sarstedt, catalog no. 06.1667.001).

Samples were separated by centrifugation (2,500 × *g*, 10 min, room temperature), and serum fractions were processed immediately and analyzed without dilution on a clinical chemistry analyzer (cobas 8000 modular analyzer, Roche). All samples were processed simultaneously, to minimize analytical variability. We evaluated (1) total CK; (2) creatinine; (3) urea; (4) AST; and (5) ALT. Reagents of *in vitro* detection kits developed for human samples (Roche, catalog nos. 05168546188, 05168589188, 05171873188, 05850819188, and 05850797188) were used and adapted for mouse samples, according to the manufacturer's instructions.

Statistical analysis

Statistical analyses were performed in Prism 10 (version 10.2.3, GraphPad Software) or in R (version 4.2.3), where data were handled using the tidyverse package (version 2.0.0; https://doi.org/10.32614/CRAN.package.tidyverse). Values are shown as individual replicates, with either media, mean and error bar, and violin and/or boxplot overlaid, as indicated. Generally, non-parametric tests were preferred; parametric tests were used when the sample size was large enough (central limit theorem) or to account for multi-factor designs. The following statistical tests were used: (1) Mann-Whitney *U* test; (2) unpaired t test; (3) Kruskal-Wallis test, followed by Dunn's multiple comparison post hoc test; (4) one-way ANOVA, followed by Tukey's multiple comparison post hoc test; (5) two-way ANOVA; and (6) three-way ANOVA, followed by Šídák's multiple comparison post hoc test. Furthermore, to account for repeated measurements from the same animal, mixed-effects linear regressions were used (followed by Tukey's multiple comparison post hoc test). Correlations were tested with Pearson's correlation coefficient, and *p* values were adjusted with Bonferroni's correction to control for multiple comparisons. Hyperbolic, sigmoidal, or linear regressions were fitted using the least-squares method, as indicated. Exact *p* values are reported, and *p* values <0.05 were considered statistically significant. The following notations were used: n.s., non-significant; SEM, standard error of the mean; and SD, standard deviation. Sample sizes were not pre-determined using statistical methods. Allocation of mice for *in vivo* experiments was randomized, and experimenters were blinded to mouse genotype and treatment group until behavioral assessments and electrophysiological recordings were concluded. For the remaining experiments, no randomization or concealment was performed. Data analysis was not performed blinded to the experimental conditions.

DATA AND CODE AVAILABILITY

All software used for the data analysis is either publicly or commercially available, and information is provided in each respective section. Sequencing data have been deposited at GEO and is accessible under GEO: GSE271487. The remaining data and code that support the findings of this study are available from the lead contacts (Tiago M. Rodrigues, tiago.rodrigues@iob.ch; Maria José Diógenes, diogenes@medicina.ulisboa.pt) upon reasonable request.

ACKNOWLEDGMENTS

We thank the CSF and tissue donors and their families for their generous contributions to science. This work was supported by Fundação para a Ciência e a Tecnologia – Ministério da Ciência, Tecnologia e Ensino Superior (FCT-MCTES, Portugal) (PTDC/SAU-NMU/110838/2009, PTDC/SAU-ENB/117013/2010, PTDC/NEU-OSD/5644/2014, PTDC/CTM-NAN/3547/2014, PTDC/MED-NEU/27946/2017), Santa Casa da Misericórdia de Lisboa (MB37–2017 and MB35-2021), the Plano de Recuperação e Resiliência (Pacto de Inovação "HfPT – Health from Portugal [Componente 5 do Plano de Recuperação e Resiliência, ao abrigo do concurso no. 02/C05-i01/2022]), the Academy of Finland (grant nos. 297211, 307416, 307866, and 315459), the Sigrid Jusélius Foundation, the Jane and Aatos Erkko Foundation, and the Strategic Neuroscience Funding of the University of Eastern Finland. It was also supported by the projects UID/BIM/50005/2019,

UIBD/04539/2020, UIDB/00511/2020, and UIDP/00511/2020, financed by FCT-MCTES, through Fundos do Orçamento de Estado. J.F.-G. was supported by FCT (SFRH/PD/BD/114441/2016) and SynaNet – Twinning Action funded by European Union's H2020 (GA-692340). T.M.R. was supported by Fundação Calouste Gulbenkian and GAPIC/Faculty of Medicine of the University of Lisbon (20130002/PEC/BG and 20150010/BG). FCT supported T.C.-C. (PD/BD/10594/2022), M.F.-M. (PD/BD/10313/2022), S.H.V. (SFRH/BPD/81627/2011), H.A.-B. (PD/BD/05182/2023), L.R.-R. (PD/BD/150344/2019), R.M.R. (SFRH/BPD/94474/2013), H.V.M. (SFRH/BPD/109347/2015), S.R.T. (PD/BD/128091/2016), M.J.R. (CEEC-IND/01741/2021), C.M.-L. (PD/BD/118238/2016), R.F.B. (PD/BD/114337/2016), C.B.F. (PD/BD/128390/2017), A.J.-S. (PD/BD/62828/2009), and I.C.M. ("Investigador FCT" [IF/00772/2013] and "Concurso de Estímulo ao Emprego Científico" [CEECIND/01670/2017]). S.I.-O. was supported by Plano de Recuperação e Resiliência (PRR) (IMM/BII/12-2023). N.A.-S. and N.M. were supported by GAPIC/Faculty of Medicine of the University of Lisbon (project ref. 20210028 and 2018009). M.M. was supported by the Sigrid Jusélius Foundation. M.B. and I.P. were funded by Proteomic Sciences. T.F.O. was supported by Neurofold and the DFG Center for Nanoscale Microscopy and Molecular Physiology of the Brain. We thank Roland Diggelmann for comments on the figures; Ilaria Gregorio, Vera Mendes, Bruno Manadas, and Francisco Enguita for technical assistance; Raquel B. Dias for advice on mEPSC data analysis; Regeneron Pharmaceuticals for the gift of BDNF; and W.W. Anderson (University of Bristol, Bristol, UK) for the data analysis (WinLTP) program. We also acknowledge (1) the Comparative Pathology Unit, Instituto de Medicina Molecular João Lobo Antunes; (2) the animal housing facilities of the Institute of Physiology, Faculty of Medicine of Lisbon; (3) the animal facility of Instituto de Medicina Molecular João Lobo Antunes; and (4) the histology facility, Instituto Gulbenkian de Ciência. Illustrations in Figure S5A and the Graphical Abstract were created in BioRender (https://www.biorender.com).

AUTHOR CONTRIBUTIONS

J.F.-G., T.F.O., C.B.D., E.C., A.d.M., A.M.S., T.M.R., and M.J.D. designed and supervised the study. J.F.-G., T.C.-C., N.A.-S., C.d.A.-B., P.M., M.M., M.T., M.B., I.P., A.H., M.H., and A.d.M. were involved in processing and analyzing the human samples. T.C.-C., S.I.-O., R.M.R., and S.R.T. prepared the primary neuronal cultures. J.F.-G., L.R.-R., and R.V. prepared the LVs. J.F.-G., T.C.-C., M.F.-M., N.A.-S., L.R.-R., C.A.-B., and A.J.-S. performed the western blot analysis. J.F.-G. prepared RNA samples for sequencing. T.M.R. performed the analysis of the bulk RNA-seq data. J.F.-G. and R.M.R. performed the MTT assays. M.F.-M., R.M.R., A.F., and T.M.R. performed the immunocytochemistry and immunofluorescence procedures. R.M.R. and T.M.R. performed the microscopy imaging. T.M.R. performed the image analyses. J.F.-G. and M.J.D. designed the TAT-TrkB peptides. J.F.-G., C.d.A.-B., V.N., and M.A.R.B.C. performed the BEB translocation assays. J.A.L., M.J.R., and M.C.P. performed the studies of the biophysical interaction of TAT-TrkB with liposomes. H.V.M. prepared and characterized the Aβ species. I.C.M. and N.C.S. performed DLS. S.H.V. and D.M.R. performed the mEPSC recordings. J.F.-G., T.M.R., T.C.-C., and S.I.-O. performed the extracellular *ex vivo* recordings (with contributions from C.M.-L., R.F.B., C.B.F., N.M., and A.C.). S.H.V., T.M.R., and J.F.-G. performed the glutamate release assays. J.F.-G., T.C.-C., M.F.-M., S.I.-O., S.R.T., C.M.-L., R.F.B., and C.B.F. performed the *in vivo* studies. T.C.-C., M.F.-M., S.I.-O., H.A.-B., and L.R.-R. harvested blood and samples for the histopathological analysis. R.P. performed the clinical chemistry measurements. T.M.R. performed the statistical analyses and prepared the figures. T.M.R. wrote the first draft of the paper, with contributions from J.F.-G., T.C.-C., M.F.-M., S.I.-O., and M.J.D. All authors reviewed and approved the final version of the manuscript.

DECLARATION OF INTERESTS

J.F.-G., M.J.D., A.J.-S., C.B.D., and A.M.S. are authors of a patent (application no. PCT/PT2021/050011; priority date: April 1, 2020) concerning the prevention of TrkB-FL cleavage as a therapeutic strategy.

SUPPLEMENTAL INFORMATION

Supplemental information can be found online at https://doi.org/10.1016/j.ymthe.2024.08.022.

REFERENCES

1. Huang, E.J., and Reichardt, L.F. (2001). Neurotrophins: roles in neuronal development and function. Annu. Rev. Neurosci. *24*, 677–736. https://doi.org/10.1146/annurev.neuro.24.1.677.

2. GBD 2019 Dementia Forecasting Collaborators (2022). Estimation of the global prevalence of dementia in 2019 and forecasted prevalence in 2050: an analysis for the Global Burden of Disease Study 2019. Lancet Public Health *7*, e105–e125. https://doi.org/10.1016/S2468-2667(21)00249-8.

3. Scheltens, P., De Strooper, B., Kivipelto, M., Holstege, H., Chételat, G., Teunissen, C.E., Cummings, J., and van der Flier, W.M. (2021). Alzheimer's disease. Lancet *397*, 1577–1590. https://doi.org/10.1016/S0140-6736(20)32205-4.

4. Masters, C.L., Simms, G., Weinman, N.A., Multhaup, G., McDonald, B.L., and Beyreuther, K. (1985). Amyloid plaque core protein in Alzheimer disease and Down syndrome. Proc. Natl. Acad. Sci. USA *82*, 4245–4249. https://doi.org/10.1073/pnas.82.12.4245.

5. Goedert, M., Wischik, C.M., Crowther, R.A., Walker, J.E., and Klug, A. (1988). Cloning and sequencing of the cDNA encoding a core protein of the paired helical filament of Alzheimer disease: identification as the microtubule-associated protein tau. Proc. Natl. Acad. Sci. USA *85*, 4051–4055. https://doi.org/10.1073/pnas.85.11.4051.

6. Hardy, J., Duff, K., Hardy, K.G., Perez-Tur, J., and Hutton, M. (1998). Genetic dissection of Alzheimer's disease and related dementias: amyloid and its relationship to tau. Nat. Neurosci. *1*, 355–358. https://doi.org/10.1038/1565.

7. Ittner, L.M., and Götz, J. (2011). Amyloid-β and tau–a toxic pas de deux in Alzheimer's disease. Nat. Rev. Neurosci. *12*, 65–72. https://doi.org/10.1038/nrn2967.

8. Gralle, M., and Ferreira, S.T. (2007). Structure and functions of the human amyloid precursor protein: the whole is more than the sum of its parts. Prog. Neurobiol. *82*, 11–32. https://doi.org/10.1016/j.pneurobio.2007.02.001.

9. Finder, V.H., and Glockshuber, R. (2007). Amyloid-beta aggregation. Neurodegener. Dis. *4*, 13–27. https://doi.org/10.1159/000100355.

10. Allen, S.J., Wilcock, G.K., and Dawbarn, D. (1999). Profound and selective loss of catalytic TrkB immunoreactivity in Alzheimer's disease. Biochem. Biophys. Res. Commun. *264*, 648–651. https://doi.org/10.1006/bbrc.1999.1561.

11. Connor, B., Young, D., Yan, Q., Faull, R.L., Synek, B., and Dragunow, M. (1997). Brain-derived neurotrophic factor is reduced in Alzheimer's disease. Brain Res. Mol. Brain Res. *49*, 71–81. https://doi.org/10.1016/s0169-328x(97)00125-3.

12. Ferrer, I., Marín, C., Rey, M.J., Ribalta, T., Goutan, E., Blanco, R., Tolosa, E., and Martí, E. (1999). BDNF and full-length and truncated TrkB expression in Alzheimer disease. Implications in therapeutic strategies. J. Neuropathol. Exp. Neurol. *58*, 729–739. https://doi.org/10.1097/00005072-199907000-00007.

13. Ginsberg, S.D., Che, S., Wuu, J., Counts, S.E., and Mufson, E.J. (2006). Down regulation of trk but not p75NTR gene expression in single cholinergic basal forebrain neurons mark the progression of Alzheimer's disease. J. Neurochem. *97*, 475–487. https://doi.org/10.1111/j.1471-4159.2006.03764.x.

14. Phillips, H.S., Hains, J.M., Armanini, M., Laramee, G.R., Johnson, S.A., and Winslow, J.W. (1991). BDNF mRNA is decreased in the hippocampus of individuals with Alzheimer's disease. Neuron *7*, 695–702. https://doi.org/10.1016/0896-6273(91)90273-3.

15. Salehi, A., Verhaagen, J., Dijkhuizen, P.A., and Swaab, D.F. (1996). Co-localization of high-affinity neurotrophin receptors in nucleus basalis of Meynert neurons and their differential reduction in Alzheimer's disease. Neuroscience *75*, 373–387. https://doi.org/10.1016/0306-4522(96)00273-4.

16. Jerónimo-Santos, A., Vaz, S.H., Parreira, S., Rapaz-Lérias, S., Caetano, A.P., Buée-Scherrer, V., Castrén, E., Valente, C.A., Blum, D., Sebastião, A.M., and Diógenes, M.J. (2015). Dysregulation of TrkB Receptors and BDNF Function by Amyloid-β Peptide is Mediated by Calpain. Cereb. Cortex *25*, 3107–3121. https://doi.org/10.1093/cercor/bhu105.

17. Tanqueiro, S.R., Ramalho, R.M., Rodrigues, T.M., Lopes, L.V., Sebastião, A.M., and Diógenes, M.J. (2018). Inhibition of NMDA Receptors Prevents the Loss of BDNF Function Induced by Amyloid β. Front. Pharmacol. *9*, 237. https://doi.org/10.3389/fphar.2018.00237.

18. Fonseca-Gomes, J., Jerónimo-Santos, A., Lesnikova, A., Casarotto, P., Castrén, E., Sebastião, A.M., and Diógenes, M.J. (2019). TrkB-ICD Fragment, Originating From BDNF Receptor Cleavage, Is Translocated to Cell Nucleus and Phosphorylates Nuclear and Axonal Proteins. Front. Mol. Neurosci. *12*, 4. https://doi.org/10.3389/fnmol.2019.00004.

19. Dittgen, T., Nimmerjahn, A., Komai, S., Licznerski, P., Waters, J., Margrie, T.W., Helmchen, F., Denk, W., Brecht, M., and Osten, P. (2004). Lentivirus-based genetic manipulations of cortical neurons and their optical and electrophysiological monitoring in vivo. Proc. Natl. Acad. Sci. USA *101*, 18206–18211. https://doi.org/10.1073/pnas.0407976101.

20. Schwarze, S.R., Ho, A., Vocero-Akbani, A., and Dowdy, S.F. (1999). In vivo protein transduction: delivery of a biologically active protein into the mouse. Science *285*, 1569–1572. https://doi.org/10.1126/science.285.5433.1569.

21. Wadia, J.S., and Dowdy, S.F. (2005). Transmembrane delivery of protein and peptide drugs by TAT-mediated transduction in the treatment of cancer. Adv. Drug Deliv. Rev. *57*, 579–596. https://doi.org/10.1016/j.addr.2004.10.005.

22. Azzarito, V., Long, K., Murphy, N.S., and Wilson, A.J. (2013). Inhibition of α-helix-mediated protein-protein interactions using designed molecules. Nat. Chem. *5*, 161–173. https://doi.org/10.1038/nchem.1568.

23. Li, S., Hou, H., Mori, T., Sawmiller, D., Smith, A., Tian, J., Wang, Y., Giunta, B., Sanberg, P.R., Zhang, S., and Tan, J. (2015). Swedish mutant APP-based BACE1 binding site peptide reduces APP β-cleavage and cerebral Aβ levels in Alzheimer's mice. Sci. Rep. *5*, 11322. https://doi.org/10.1038/srep11322.

24. Rao, T., Ruiz-Gómez, G., Hill, T.A., Hoang, H.N., Fairlie, D.P., and Mason, J.M. (2013). Truncated and helix-constrained peptides with high affinity and specificity for the cFos coiled-coil of AP-1. PLoS One *8*, e59415. https://doi.org/10.1371/journal.pone.0059415.

25. Chen, X., Zaro, J.L., and Shen, W.-C. (2013). Fusion protein linkers: property, design and functionality. Adv. Drug Deliv. Rev. *65*, 1357–1369. https://doi.org/10.1016/j.addr.2012.09.039.

26. Neves, V., Aires-da-Silva, F., Morais, M., Gano, L., Ribeiro, E., Pinto, A., Aguiar, S., Gaspar, D., Fernandes, C., Correia, J.D.G., and Castanho, M.A.R.B. (2017). Novel Peptides Derived from Dengue Virus Capsid Protein Translocate Reversibly the Blood-Brain Barrier through a Receptor-Free Mechanism. ACS Chem. Biol. *12*, 1257–1268. https://doi.org/10.1021/acschembio.7b00087.

27. Kramár, E.A., Babayan, A.H., Gavin, C.F., Cox, C.D., Jafari, M., Gall, C.M., Rumbaugh, G., and Lynch, G. (2012). Synaptic evidence for the efficacy of spaced learning. Proc. Natl. Acad. Sci. USA *109*, 5121–5126. https://doi.org/10.1073/pnas.1120700109.

28. Fontinha, B.M., Diógenes, M.J., Ribeiro, J.A., and Sebastião, A.M. (2008). Enhancement of long-term potentiation by brain-derived neurotrophic factor requires adenosine A2A receptor activation by endogenous adenosine. Neuropharmacology *54*, 924–933. https://doi.org/10.1016/j.neuropharm.2008.01.011.

29. Oakley, H., Cole, S.L., Logan, S., Maus, E., Shao, P., Craft, J., Guillozet-Bongaarts, A., Ohno, M., Disterhoft, J., Van Eldik, L., et al. (2006). Intraneuronal beta-amyloid aggregates, neurodegeneration, and neuron loss in transgenic mice with five familial Alzheimer's disease mutations: potential factors in amyloid plaque formation. J. Neurosci. *26*, 10129–10140. https://doi.org/10.1523/JNEUROSCI.1202-06.2006.

30. Ohno, M., Chang, L., Tseng, W., Oakley, H., Citron, M., Klein, W.L., Vassar, R., and Disterhoft, J.F. (2006). Temporal memory deficits in Alzheimer's mouse models: rescue by genetic deletion of BACE1. Eur. J. Neurosci. *23*, 251–260. https://doi.org/10.1111/j.1460-9568.2005.04551.x.

31. Forner, S., Kawauchi, S., Balderrama-Gutierrez, G., Kramár, E.A., Matheos, D.P., Phan, J., Javonillo, D.I., Tran, K.M., Hingco, E., da Cunha, C., et al. (2021). Systematic phenotyping and characterization of the 5xFAD mouse model of Alzheimer's disease. Sci. Data *8*, 270. https://doi.org/10.1038/s41597-021-01054-y.

32. Jawhar, S., Trawicka, A., Jenneckens, C., Bayer, T.A., and Wirths, O. (2012). Motor deficits, neuron loss, and reduced anxiety coinciding with axonal degeneration and intraneuronal Aβ aggregation in the 5XFAD mouse model of Alzheimer's disease. Neurobiol. Aging *33*, 196.e29–196.e40. https://doi.org/10.1016/j.neurobiolaging.2010.05.027.

33. Rice, R.A., Spangenberg, E.E., Yamate-Morgan, H., Lee, R.J., Arora, R.P.S., Hernandez, M.X., Tenner, A.J., West, B.L., and Green, K.N. (2015). Elimination of Microglia Improves Functional Outcomes Following Extensive Neuronal Loss in the Hippocampus. J. Neurosci. *35*, 9977–9989. https://doi.org/10.1523/JNEUROSCI.0336-15.2015.

34. Kimura, R., and Ohno, M. (2009). Impairments in remote memory stabilization precede hippocampal synaptic and cognitive failures in 5XFAD Alzheimer mouse model. Neurobiol. Dis. *33*, 229–235. https://doi.org/10.1016/j.nbd.2008.10.006.

35. Crouzin, N., Baranger, K., Cavalier, M., Marchalant, Y., Cohen-Solal, C., Roman, F.S., Khrestchatisky, M., Rivera, S., Féron, F., and Vignes, M. (2013). Area-specific alterations of synaptic plasticity in the 5XFAD mouse model of Alzheimer's disease: dissociation between somatosensory cortex and hippocampus. PLoS One *8*, e74667. https://doi.org/10.1371/journal.pone.0074667.

36. Kanno, T., Tsuchiya, A., and Nishizaki, T. (2014). Hyperphosphorylation of Tau at Ser396 occurs in the much earlier stage than appearance of learning and memory disorders in 5XFAD mice. Behav. Brain Res. *274*, 302–306. https://doi.org/10.1016/j.bbr.2014.08.034.

37. Kourti, M., and Metaxas, A. (2024). A systematic review and meta-analysis of tau phosphorylation in mouse models of familial Alzheimer's disease. Neurobiol. Dis. *192*, 106427. https://doi.org/10.1016/j.nbd.2024.106427.

38. Loeb, W.F., and Quimby, F.W. (1999). The Clinical Chemistry of Laboratory Animals, 2nd Edition (Taylor and Francis).

39. Tejeda, G.S., Esteban-Ortega, G.M., San Antonio, E., Vidaurre, Ó.G., and Díaz-Guerra, M. (2019). Prevention of excitotoxicity-induced processing of BDNF receptor TrkB-FL leads to stroke neuroprotection. EMBO Mol. Med. *11*, e9950. https://doi.org/10.15252/emmm.201809950.

40. Chen, Q.S., Kagan, B.L., Hirakura, Y., and Xie, C.W. (2000). Impairment of hippocampal long-term potentiation by Alzheimer amyloid beta-peptides. J. Neurosci. Res. *60*, 65–72. https://doi.org/10.1002/(SICI)1097-4547(20000401)60:1<65::AID-JNR7>3.0.CO;2-Q.

41. Ferreira, S.T., and Klein, W.L. (2011). The Aβ oligomer hypothesis for synapse failure and memory loss in Alzheimer's disease. Neurobiol. Learn. Mem. *96*, 529–543. https://doi.org/10.1016/j.nlm.2011.08.003.

42. Mucke, L., and Selkoe, D.J. (2012). Neurotoxicity of amyloid β-protein: synaptic and network dysfunction. Cold Spring Harb. Perspect. Med. *2*, a006338. https://doi.org/10.1101/cshperspect.a006338.

43. Diógenes, M.J., Costenla, A.R., Lopes, L.V., Jerónimo-Santos, A., Sousa, V.C., Fontinha, B.M., Ribeiro, J.A., and Sebastião, A.M. (2011). Enhancement of LTP in aged rats is dependent on endogenous BDNF. Neuropsychopharmacology *36*, 1823–1836. https://doi.org/10.1038/npp.2011.64.

44. Cardozo, A.K., Buchillier, V., Mathieu, M., Chen, J., Ortis, F., Ladrière, L., Allaman-Pillet, N., Poirot, O., Kellenberger, S., Beckmann, J.S., et al. (2007). Cell-permeable peptides induce dose- and length-dependent cytotoxic effects. Biochim. Biophys. Acta *1768*, 2222–2234. https://doi.org/10.1016/j.bbamem.2007.06.003.

45. Roy, E.R., Wang, B., Wan, Y.-W., Chiu, G., Cole, A., Yin, Z., Propson, N.E., Xu, Y., Jankowsky, J.L., Liu, Z., et al. (2020). Type I interferon response drives neuroinflammation and synapse loss in Alzheimer disease. J. Clin. Invest. *130*, 1912–1930. https://doi.org/10.1172/JCI133737.

46. Li, Y., Zhu, K., Li, N., Wang, X., Xiao, X., Li, L., Li, L., He, Y., Zhang, J., Wo, J., et al. (2021). Reversible GABAergic dysfunction involved in hippocampal hyperactivity predicts early-stage Alzheimer disease in a mouse model. Alzheimers Res. Ther. *13*, 114. https://doi.org/10.1186/s13195-021-00859-8.

47. Zheng, J., Li, H.-L., Tian, N., Liu, F., Wang, L., Yin, Y., Yue, L., Ma, L., Wan, Y., and Wang, J.-Z. (2020). Interneuron Accumulation of Phosphorylated tau Impairs Adult Hippocampal Neurogenesis by Suppressing GABAergic Transmission. Cell Stem Cell *26*, 331–345.e6. https://doi.org/10.1016/j.stem.2019.12.015.

48. Hanseeuw, B.J., Betensky, R.A., Jacobs, H.I.L., Schultz, A.P., Sepulcre, J., Becker, J.A., Cosio, D.M.O., Farrell, M., Quiroz, Y.T., Mormino, E.C., et al. (2019). Association of Amyloid and Tau With Cognition in Preclinical Alzheimer Disease: A Longitudinal Study. JAMA Neurol. *76*, 915–924. https://doi.org/10.1001/jamaneurol.2019.1424.

49. Ossenkoppele, R., Smith, R., Mattsson-Carlgren, N., Groot, C., Leuzy, A., Strandberg, O., Palmqvist, S., Olsson, T., Jögi, J., Stormrud, E., et al. (2021). Accuracy of Tau Positron Emission Tomography as a Prognostic Marker in Preclinical and Prodromal Alzheimer Disease: A Head-to-Head Comparison Against Amyloid Positron Emission Tomography and Magnetic Resonance Imaging. JAMA Neurol. *78*, 961–971. https://doi.org/10.1001/jamaneurol.2021.1858.

50. Bellaver, B., Povala, G., Ferreira, P.C.L., Ferrari-Souza, J.P., Leffa, D.T., Lussier, F.Z., Benedet, A.L., Ashton, N.J., Triana-Baltzer, G., Kolb, H.C., et al. (2023). Astrocyte

reactivity influences amyloid-β effects on tau pathology in preclinical Alzheimer's disease. Nat. Med. *29*, 1775–1781. https://doi.org/10.1038/s41591-023-02380-x.

51. Graham, W.V., Bonito-Oliva, A., and Sakmar, T.P. (2017). Update on Alzheimer's Disease Therapy and Prevention Strategies. Annu. Rev. Med. *68*, 413–430. https://doi.org/10.1146/annurev-med-042915-103753.

52. Danelon, V., Montroull, L.E., Unsain, N., Barker, P.A., and Mascó, D.H. (2016). Calpain-dependent truncated form of TrkB-FL increases in neurodegenerative processes. Mol. Cell. Neurosci. *75*, 81–92. https://doi.org/10.1016/j.mcn.2016.07.002.

53. Gomes, J.R., Costa, J.T., Melo, C.V., Felizzi, F., Monteiro, P., Pinto, M.J., Inácio, A.R., Wieloch, T., Almeida, R.D., Grãos, M., and Duarte, C.B. (2012). Excitotoxicity downregulates TrkB.FL signaling and upregulates the neuroprotective truncated TrkB receptors in cultured hippocampal and striatal neurons. J. Neurosci. *32*, 4610–4622. https://doi.org/10.1523/JNEUROSCI.0374-12.2012.

54. Vidaurre, O.G., Gascón, S., Deogracias, R., Sobrado, M., Cuadrado, E., Montaner, J., Rodríguez-Peña, A., and Díaz-Guerra, M. (2012). Imbalance of neurotrophin receptor isoforms TrkB-FL/TrkB-T1 induces neuronal death in excitotoxicity. Cell Death Dis. *3*, e256. https://doi.org/10.1038/cddis.2011.143.

55. Goll, D.E., Thompson, V.F., Li, H., Wei, W., and Cong, J. (2003). The calpain system. Physiol. Rev. *83*, 731–801. https://doi.org/10.1152/physrev.00029.2002.

56. Ono, Y., Saido, T.C., and Sorimachi, H. (2016). Calpain research for drug discovery: challenges and potential. Nat. Rev. Drug Discov. *15*, 854–876. https://doi.org/10.1038/nrd.2016.212.

57. Albert, M.S., DeKosky, S.T., Dickson, D., Dubois, B., Feldman, H.H., Fox, N.C., Gamst, A., Holtzman, D.M., Jagust, W.J., Petersen, R.C., et al. (2011). The diagnosis of mild cognitive impairment due to Alzheimer's disease: recommendations from the National Institute on Aging-Alzheimer's Association workgroups on diagnostic guidelines for Alzheimer's disease. Alzheimers Dement. *7*, 270–279. https://doi.org/10.1016/j.jalz.2011.03.008.

58. Rascovsky, K., Hodges, J.R., Knopman, D., Mendez, M.F., Kramer, J.H., Neuhaus, J., van Swieten, J.C., Seelaar, H., Dopper, E.G.P., Onyike, C.U., et al. (2011). Sensitivity of revised diagnostic criteria for the behavioural variant of frontotemporal dementia. Brain. *134*, 2456–2477. https://doi.org/10.1093/brain/awr179.

59. Teunissen, C.E., Tumani, H., Engelborghs, S., and Mollenhauer, B. (2014). Biobanking of CSF: international standardization to optimize biomarker development. Clin. Biochem. *47*, 288–292. https://doi.org/10.1016/j.clinbiochem.2013.12.024.

60. Marttinen, M., Paananen, J., Neme, A., Mitra, V., Takalo, M., Natunen, T., Paldanius, K.M.A., Mäkinen, P., Bremang, M., Kurki, M.I., et al. (2019). A multiomic approach to characterize the temporal sequence in Alzheimer's disease-related pathology. Neurobiol. Dis. *124*, 454–468. https://doi.org/10.1016/j.nbd.2018.12.009.

61. Braak, H., Alafuzoff, I., Arzberger, T., Kretzschmar, H., and Del Tredici, K. (2006). Staging of Alzheimer disease-associated neurofibrillary pathology using paraffin sections and immunocytochemistry. Acta Neuropathol. *112*, 389–404. https://doi.org/10.1007/s00401-006-0127-z.

62. Natunen, T., Parrado, A.R., Helisalmi, S., Pursiheimo, J.-P., Sarajärvi, T., Mäkinen, P., Kurkinen, K.M.A., Mullin, K., Alafuzoff, I., Haapasalo, A., et al. (2013). Elucidation of the BACE1 regulating factor GGA3 in Alzheimer's disease. J. Alzheimers Dis. *37*, 217–232. https://doi.org/10.3233/JAD-130104.

63. Schindelin, J., Arganda-Carreras, I., Frise, E., Kaynig, V., Longair, M., Pietzsch, T., Preibisch, S., Rueden, C., Saalfeld, S., Schmid, B., et al. (2012). Fiji: an open-source platform for biological-image analysis. Nat. Methods *9*, 676–682. https://doi.org/10.1038/nmeth.2019.

64. Kieslich, C.A., Smadbeck, J., Khoury, G.A., and Floudas, C.A. (2016). conSSert: Consensus SVM Model for Accurate Prediction of Ordered Secondary Structure. J. Chem. Inf. Model. *56*, 455–461. https://doi.org/10.1021/acs.jcim.5b00566.

65. Pollastri, G., Przybylski, D., Rost, B., and Baldi, P. (2002). Improving the prediction of protein secondary structure in three and eight classes using recurrent neural networks and profiles. Proteins *47*, 228–235. https://doi.org/10.1002/prot.10082.

66. Lamiable, A., Thévenet, P., Rey, J., Vavrusa, M., Derreumaux, P., and Tufféry, P. (2016). PEP-FOLD3: faster de novo structure prediction for linear peptides in solution and in complex. Nucleic Acids Res. *44*, W449–W454. https://doi.org/10.1093/nar/gkw329.

67. Gamir-Morralla, A., López-Menéndez, C., Ayuso-Dolado, S., Tejeda, G.S., Montaner, J., Rosell, A., Iglesias, T., and Díaz-Guerra, M. (2015). Development of a neuroprotective peptide that preserves survival pathways by preventing Kidins220/ARMS calpain processing induced by excitotoxicity. Cel Death Dis. *6*, e1939. https://doi.org/10.1038/cddis.2015.307.

68. Dias, R.B., Rodrigues, T.M., Rombo, D.M., Ribeiro, F.F., Rodrigues, J., McGarvey, J., Orcinha, C., Henley, J.M., and Sebastião, A.M. (2018). Erythropoietin Induces Homeostatic Plasticity at Hippocampal Synapses. Cereb. Cortex *28*, 2795–2809. https://doi.org/10.1093/cercor/bhx159.

69. Koskinen, M., and Hotulainen, P. (2014). Measuring F-actin properties in dendritic spines. Front. Neuroanat. *8*, 74. https://doi.org/10.3389/fnana.2014.00074.

70. Barrett, T., Wilhite, S.E., Ledoux, P., Evangelista, C., Kim, I.F., Tomashevsky, M., Marshall, K.A., Phillippy, K.H., Sherman, P.M., Holko, M., et al. (2013). NCBI GEO: archive for functional genomics data sets–update. Nucleic Acids Res. *41*, D991–D995. https://doi.org/10.1093/nar/gks1193.

71. Dobin, A., Davis, C.A., Schlesinger, F., Drenkow, J., Zaleski, C., Jha, S., Batut, P., Chaisson, M., and Gingeras, T.R. (2013). STAR: ultrafast universal RNA-seq aligner. Bioinformatics *29*, 15–21. https://doi.org/10.1093/bioinformatics/bts635.

72. Hoffman, G.E., and Roussos, P. (2021). Dream: powerful differential expression analysis for repeated measures designs. Bioinformatics *37*, 192–201. https://doi.org/10.1093/bioinformatics/btaa687.

73. Graziano, A.M., and Raulin, M.L. (2014). Research Methods: A Process of Inquiry, 9th Edition (Pearson Education).

74. Zhang, H. (2017). Thin-Film Hydration Followed by Extrusion Method for Liposome Preparation. Methods Mol. Biol. *1522*, 17–22. https://doi.org/10.1007/978-1-4939-6591-5_2.

75. Magalhães, L.M., Nunes, C., Lúcio, M., Segundo, M.A., Reis, S., and Lima, J.L.F.C. (2010). High-throughput microplate assay for the determination of drug partition coefficients. Nat. Protoc. *5*, 1823–1830. https://doi.org/10.1038/nprot.2010.137.

76. Andrade, S., Ramalho, M.J., Loureiro, J.A., and Pereira, M.C. (2019). Interaction of natural compounds with biomembrane models: A biophysical approach for the Alzheimer's disease therapy. Colloids Surf. B Biointerfaces *180*, 83–92. https://doi.org/10.1016/j.colsurfb.2019.04.019.

77. Michel, N., Fabiano, A.-S., Polidori, A., Jack, R., and Pucci, B. (2006). Determination of phase transition temperatures of lipids by light scattering. Chem. Phys. Lipids *139*, 11–19. https://doi.org/10.1016/j.chemphyslip.2005.09.003.

78. Giuffrida, M.L., Caraci, F., Pignataro, B., Cataldo, S., De Bona, P., Bruno, V., Molinaro, G., Pappalardo, G., Messina, A., Palmigiano, A., et al. (2009). Beta-amyloid monomers are neuroprotective. J. Neurosci. *29*, 10582–10587. https://doi.org/10.1523/JNEUROSCI.1736-09.2009.

79. Vicente Miranda, H., Szego, É.M., Oliveira, L.M.A., Breda, C., Darendelioglu, E., de Oliveira, R.M., Ferreira, D.G., Gomes, M.A., Rott, R., Oliveira, M., et al. (2017). Glycation potentiates α-synuclein-associated neurodegeneration in synucleinopathies. Brain. *140*, 1399–1419. https://doi.org/10.1093/brain/awx056.

80. Schiff, S.J., and Somjen, G.G. (1985). The effects of temperature on synaptic transmission in hippocampal tissue slices. Brain Res. *345*, 279–284. https://doi.org/10.1016/0006-8993(85)91004-2.

81. Dahlgren, K.N., Manelli, A.M., Stine, W.B., Baker, L.K., Krafft, G.A., and LaDu, M.J. (2002). Oligomeric and fibrillar species of amyloid-beta peptides differentially affect neuronal viability. J. Biol. Chem. *277*, 32046–32053. https://doi.org/10.1074/jbc.M201750200.

82. Ripoli, C., Piacentini, R., Riccardi, E., Leone, L., Li Puma, D.D., Bitan, G., and Grassi, C. (2013). Effects of different amyloid β-protein analogues on synaptic function. Neurobiol. Aging *34*, 1032–1044. https://doi.org/10.1016/j.neurobiolaging.2012.06.027.

83. Karran, E., Mercken, M., and De Strooper, B. (2011). The amyloid cascade hypothesis for Alzheimer's disease: an appraisal for the development of therapeutics. Nat. Rev. Drug Discov. *10*, 698–712. https://doi.org/10.1038/nrd3505.

84. Alonso, M., Medina, J.H., and Pozzo-Miller, L. (2004). ERK1/2 activation is necessary for BDNF to increase dendritic spine density in hippocampal CA1 pyramidal neurons. Learn. Mem. *11*, 172–178. https://doi.org/10.1101/lm.67804.

85. Rodrigues, T.M., Jerónimo-Santos, A., Sebastião, A.M., and Diógenes, M.J. (2014). Adenosine A(2A) Receptors as novel upstream regulators of BDNF-mediated attenuation of hippocampal Long-Term Depression (LTD). Neuropharmacology *79*, 389–398. https://doi.org/10.1016/j.neuropharm.2013.12.010.

86. Anderson, W.W., and Collingridge, G.L. (2001). The LTP Program: a data acquisition program for on-line analysis of long-term potentiation and other synaptic events. J. Neurosci. Methods *108*, 71–83. https://doi.org/10.1016/s0165-0270(01)00374-0.

87. Vaz, S.H., Lérias, S.R., Parreira, S., Diógenes, M.J., and Sebastião, A.M. (2015). Adenosine A2A receptor activation is determinant for BDNF actions upon GABA and glutamate release from rat hippocampal synaptosomes. Purinergic Signal. *11*, 607–612. https://doi.org/10.1007/s11302-015-9476-1.

88. Raiteri, L., and Raiteri, M. (2000). Synaptosomes still viable after 25 years of superfusion. Neurochem. Res. *25*, 1265–1274. https://doi.org/10.1023/a:1007648229795.

89. Wu, Y., Luo, X., Liu, X., Liu, D., Wang, X., Guo, Z., Zhu, L., Tian, Q., Yang, X., and Wang, J.-Z. (2015). Intraperitoneal Administration of a Novel TAT-BDNF Peptide Ameliorates Cognitive Impairments via Modulating Multiple Pathways in Two Alzheimer's Rodent Models. Sci. Rep. *5*, 15032. https://doi.org/10.1038/srep15032.

90. Brittain, J.M., Chen, L., Wilson, S.M., Brustovetsky, T., Gao, X., Ashpole, N.M., Molosh, A.I., You, H., Hudmon, A., Shekhar, A., et al. (2011). Neuroprotection against traumatic brain injury by a peptide derived from the collapsin response mediator protein 2 (CRMP2). J. Biol. Chem. *286*, 37778–37792. https://doi.org/10.1074/jbc.M111.255455.

91. Cao, G., Pei, W., Ge, H., Liang, Q., Luo, Y., Sharp, F.R., Lu, A., Ran, R., Graham, S.H., and Chen, J. (2002). In Vivo Delivery of a Bcl-xL Fusion Protein Containing the TAT Protein Transduction Domain Protects against Ischemic Brain Injury and Neuronal Apoptosis. J. Neurosci. *22*, 5423–5431. https://doi.org/10.1523/JNEUROSCI.22-13-05423.2002.

92. Zhu, H., Wang, X., Wallack, M., Li, H., Carreras, I., Dedeoglu, A., Hur, J.-Y., Zheng, H., Li, H., Fine, R., et al. (2015). Intraperitoneal injection of the pancreatic peptide amylin potently reduces behavioral impairment and brain amyloid pathology in murine models of Alzheimer's disease. Mol. Psychiatry *20*, 252–262. https://doi.org/10.1038/mp.2014.17.

93. Mi, Y.-J., Chen, H., Guo, N., Sun, M.-Y., Zhao, Z.-H., Gao, X.-C., Wang, X.-L., Zhang, R.-S., Zhou, J.-B., and Gou, X.-C. (2017). Inhibition of PirB Activity by TAT-PEP Improves Mouse Motor Ability and Cognitive Behavior. Front. Aging Neurosci. *9*, 199. https://doi.org/10.3389/fnagi.2017.00199.

94. Antunes, M., and Biala, G. (2012). The novel object recognition memory: neurobiology, test procedure, and its modifications. Cogn. Process. *13*, 93–110. https://doi.org/10.1007/s10339-011-0430-z.

95. Mouro, F.M., Kőfalvi, A., André, L.A., Baqi, Y., Müller, C.E., Ribeiro, J.A., and Sebastião, A.M. (2019). Memory deficits induced by chronic cannabinoid exposure are prevented by adenosine A2AR receptor antagonism. Neuropharmacology *155*, 10–21. https://doi.org/10.1016/j.neuropharm.2019.05.003.

96. Batalha, V.L., Pego, J.M., Fontinha, B.M., Costenla, A.R., Valadas, J.S., Baqi, Y., Radjainia, H., Müller, C.E., Sebastião, A.M., and Lopes, L.V. (2013). Adenosine A(2A) receptor blockade reverts hippocampal stress-induced deficits and restores corticosterone circadian oscillation. Mol. Psychiatry *18*, 320–331. https://doi.org/10.1038/mp.2012.8.

97. Morris, R.G., Garrud, P., Rawlins, J.N., and O'Keefe, J. (1982). Place navigation impaired in rats with hippocampal lesions. Nature *297*, 681–683. https://doi.org/10.1038/297681a0.

98. Keenan, C.M., Baker, J.F., Bradley, A.E., Goodman, D.G., Harada, T., Herbert, R., Kaufmann, W., Kellner, R., Mahler, B., Meseck, E., et al. (2015). International Harmonization of Nomenclature and Diagnostic Criteria (INHAND) progress to date and future plans. J. Toxicol. Pathol. *28*, 51–53. https://doi.org/10.1293/tox.2014-0049.